

RF-TRAPPED CHIP SCALE HELIUM ION PUMP (RFT-CHIP)

Yogesh Gianchandani, et al.

**The Regents of the University of Michigan
Office of Research and Sponsored Projects
503 Thompson St.
Ann Arbor, MI 48109-1340**

06 April 2016

Final Report

APPROVED FOR PUBLIC RELEASE; DISTRIBUTION IS UNLIMITED.



**AIR FORCE RESEARCH LABORATORY
Space Vehicles Directorate
3550 Aberdeen Ave SE
AIR FORCE MATERIEL COMMAND
KIRTLAND AIR FORCE BASE, NM 87117-5776**

DTIC COPY

NOTICE AND SIGNATURE PAGE

Using Government drawings, specifications, or other data included in this document for any purpose other than Government procurement does not in any way obligate the U.S. Government. The fact that the Government formulated or supplied the drawings, specifications, or other data does not license the holder or any other person or corporation; or convey any rights or permission to manufacture, use, or sell any patented invention that may relate to them.

This report is the result of contracted fundamental research which is exempt from public affairs security and policy review in accordance with AFI 61-201, paragraph 2.3.5.1. This report is available to the general public, including foreign nationals. Copies may be obtained from the Defense Technical Information Center (DTIC) (<http://www.dtic.mil>).

AFRL-RV-PS-TR-2017-0164 HAS BEEN REVIEWED AND IS APPROVED FOR
PUBLICATION IN ACCORDANCE WITH ASSIGNED DISTRIBUTION STATEMENT.

//SIGNED//

Dr. Spencer E. Olson
Program Manager, AFRL/RVBYE

//SIGNED//

Dr. Thomas R. Caudill, Acting Chief
AFRL Battlespace Environment Division

This report is published in the interest of scientific and technical information exchange, and its publication does not constitute the Government's approval or disapproval of its ideas or findings.

REPORT DOCUMENTATION PAGE				Form Approved OMB No. 0704-0188	
Public reporting burden for this collection of information is estimated to average 1 hour per response, including the time for reviewing instructions, searching existing data sources, gathering and maintaining the data needed, and completing and reviewing this collection of information. Send comments regarding this burden estimate or any other aspect of this collection of information, including suggestions for reducing this burden to Department of Defense, Washington Headquarters Services, Directorate for Information Operations and Reports (0704-0188), 1215 Jefferson Davis Highway, Suite 1204, Arlington, VA 22202-4302. Respondents should be aware that notwithstanding any other provision of law, no person shall be subject to any penalty for failing to comply with a collection of information if it does not display a currently valid OMB control number. PLEASE DO NOT RETURN YOUR FORM TO THE ABOVE ADDRESS.					
1. REPORT DATE (DD-MM-YYYY) 06-04-2016		2. REPORT TYPE Final Report		3. DATES COVERED (From - To) 27 Aug 2014 – 06 Apr 2016	
4. TITLE AND SUBTITLE RF-Trapped Chip Scale Helium Ion Pump (RFT-CHIP)				5a. CONTRACT NUMBER	
				5b. GRANT NUMBER FA9453-14-1-0347	
				5c. PROGRAM ELEMENT NUMBER 62601F	
6. AUTHOR(S) Yogesh Gianchandani, Mark Kushner, Scott Green, Aram Markosyan, and Shiyang Deng				5d. PROJECT NUMBER 1010	
				5e. TASK NUMBER PPM00025368	
				5f. WORK UNIT NUMBER EF129740	
7. PERFORMING ORGANIZATION NAME(S) AND ADDRESS(ES) The Regents of the University of Michigan Office of Research and Sponsored Projects 503 Thompson St. Ann Arbor, MI 48109-1340				8. PERFORMING ORGANIZATION REPORT NUMBER	
9. SPONSORING / MONITORING AGENCY NAME(S) AND ADDRESS(ES) Air Force Research Laboratory Space Vehicles Directorate 3550 Aberdeen Avenue SE Kirtland AFB, NM 87117-5776				10. SPONSOR/MONITOR'S ACRONYM(S) AFRL/RVBYE	
				11. SPONSOR/MONITOR'S REPORT NUMBER(S) AFRL-RV-PS-TR-2017-0164	
12. DISTRIBUTION / AVAILABILITY STATEMENT Approved for public release; distribution is unlimited.					
13. SUPPLEMENTARY NOTES					
14. ABSTRACT A miniaturized (~1 cc) magnet-less RF electron trap for a helium ion pump is studied, addressing challenges associated with active pumping of atomic microsystems at low pressures (~1 nanoTorr). Two tasks are described: experimental verification of electron trapping, and numerical parametric modeling of electron trapping and ionization. It is found experimentally that the steady state floating potentials on electrodes near the trap become more negative after applying certain RF power levels, demonstrating electron trapping. The electron density within the trap is estimated via numerical modeling as ~1000x the density in the electron beam. Estimated Ionization rates are as high as 60E6/cc/s.					
15. SUBJECT TERMS microsystems, vacuum pump, ion pump, electron trap, magnet-less, MEMS, radiofrequency					
16. SECURITY CLASSIFICATION OF:			17. LIMITATION OF ABSTRACT Unlimited	18. NUMBER OF PAGES 38	19a. NAME OF RESPONSIBLE PERSON Dr. Spencer E. Olson
a. REPORT Unclassified	b. ABSTRACT Unclassified	c. THIS PAGE Unclassified			19b. TELEPHONE NUMBER (include area code)

This page is intentionally left blank.

Table of Contents

1.0 Project overview	1
<i>1.1 Motivation and challenges</i>	1
<i>1.2 Concept</i>	2
2.0 Significant accomplishments in Phase I	5
3.0 Task by task account of progress	6
3.A Task A – Experimental proof of concept	6
3.A.1 – Analytical model of RF electron trapping concept	6
3.A.2 – Electron trapping module (ETM) design and fabrication	7
3.A.3 – Vacuum test setup	8
3.A.4 – ETM RF characterization and modeling	10
3.A.5 – ETM RF electron trapping characterization	14
3.A.6 – Ionization rate measurements	17
3.A.7 – Second generation device – Enhanced efficiency electron trapping module	18
3.A.8 – Fabricated and assembled E ³ TM	20
3.A.9 – Modification of vacuum testing setup	20
3.B Task B – Detailed numerical and parametric modeling	22
3.B.1 – Model description	22
3.B.2 – Results	24
4.0 Conclusions	28
5.0 Discussion and future potential	28
References	30

List of Figures and Tables

Figures

1: Miniaturized ion pump concept: 3D model (left), 2D schematic (center), detailed view of grid cathode (right)	2
2: Analytical model of RF electron trapping	6
3: Schematic and exploded view of electron trapping module (ETM)	7
4: a) The ETM consists of two perforated stainless steel RF electrodes, separated by a U-shaped stainless steel chassis with two U-shaped ceramic sheets for electrical isolation. b) U-shaped ceramic sheet. c) Perforated stainless steel RF electrode. d) U-shaped stainless steel chassis	8
5: The vacuum setup consists of a commercial combination diaphragm/turbo pump (Agilent Mini-TASK AG81) and a commercial sputter ion pump (Agilent, 20L/s Valcon Pump) capable of pumping down/to pump down to 10 nanoTorr	9
6: Testing setup	10
7: The de-embedded impedance of ETM ZL from RFA from 20 MHz to 300 MHz with all electrodes except RFA grounded	11
8: The equivalent circuit model of ETM	11
9: The series resonance associated with each branch in the circuit is determined experimentally by loading one branch with an inductor (225 nH), and identifying the shift in the measured impedance spectrum	12
10: The SPICE simulated ETM impedance magnitude compared with the de-embedded ETM impedance magnitude	13
11: Three colored curves indicate peak RF voltage $ V_{RF} $ developed at RFA across the frequency range with different output RF power P_{out}	14
12: Electrical testing setup for RF electron trapping	15
13: The SSFPs measured across the capacitors in series with the Collector 1 and Chassis electrodes during RF electron trapping at different RF power levels with a fixed RF frequency of 143.6 MHz	16
14: The SSFPs across the capacitors associated with the Collector 1 and Chassis during RF trapping at different RF frequencies with a fixed output RF power of 0.836 W	17
15: (Left) The testing configuration to investigate the gas ionization of the ETM. R1 is a 150 Ω high power resistor (Caddock Electronics MP915-150-1%, 15 W rated power), and R2 is a standard 1 M Ω resistor. (Right) Timing diagram of the control voltages at TTL port of the high power RF switch (S1) and gates of two Power MOSFETs (M1 and M2) during one ion extraction and RF electron trapping cycle	17
16: The E ³ TM consists of two titanium grid electrodes and a tantalum sorption layer, and is built on top of a 9-pin, subminiature-C 1.33" CF feedthrough	19
17: Fabricated and assembled E ³ TM	20
18: The modified vacuum setup for E ³ TM is shown in the dashed box	20
19: Customized electron gun along with the 1.33" spherical cube vacuum chamber	21
20: Speedup in HPEM code solutions via multi-core processing	23
21: Schematic of the electron trap geometry used in the HPEM model	23
22: Plasma properties for the nominal case conditions (He, 80 nTorr, 150 MHz, 150 V, 15 eV, 40 μ A)	24
23: Plasma properties for the nominal case conditions (He, 80 nTorr, 150 MHz, 150 V, 15 eV, 40 μ A)	25
24: Electron trapping for gas pressures of 40, 80, and 120 nTorr (He, 150 MHz, 150 V, 15 eV, 40 μ A)	25
25: Electron impact ionization sources by beam electrons for the initial beam energies of (a) 5 eV, (b) 15 eV, (c) 30 eV, and (d) 60 eV (He, 80 nTorr, 150 MHz, 150 V, 40 μ A)	26
26: (left) Electron densities as a function of height on $x = 0$ cm for different electron beam currents. (right) Peak electron density as a function of electron beam current (He, 80 nTorr, 150 MHz, 150 V)	27
27: Peak electron density as a function of applied RF voltage (He, 80 nTorr, 150 MHz, 15 eV, 40 μ A)	27
28: Peak electron density as a function of kf for RF frequencies of 50, 100, 150, 200, and 250 MHz (He, 80 nTorr, 15 eV, 40 μ A)	28

Table

1: Summary of series resonant frequencies, capacitances, inductances, and resistances of seven branches in the equivalent circuit model	12
---	----

1.0 Project overview

1.1 Motivation and challenges

On-board vacuum generation and maintenance are essential for microsystems that require very precise control over package pressure over long periods of deployment. For example, miniaturized atomic inertial sensors require low operating pressure to minimize spurious between the atomic vapor species and gas molecules [Zoo92, Bor02]. However, the pressure of a conventional hermetically sealed package can increase significantly due to leakage paths into the cavity and outgassing from interior surfaces of the vacuum cavity. In cases like atomic microsystems, which require ultra-high vacuum (UHV, $<1\ \mu\text{Torr}$ ($0.133\ \text{mPa}$)), even a combination of passive approaches like the use of low leakage packaging and getters is insufficient over a reasonable deployment interval. In particular, gettering of atomic helium is a challenge: helium that diffuses into the package remains unabsorbed by the getters.

In contrast to conventional passive vacuum maintenance methods, a miniaturized active pump can potentially provide a stable vacuum environment at the chip-scale. However, ultra-high vacuum levels are not practically realized by chip-scale mechanical roughing pumps, as the compressibility of the gas is too high for such pumps to work in this pressure regime. Such vacuum levels are also not easily met by chip-scale thermal transpiration (Knudsen) pumps [An13], as the required dimensional scaling of molecular flow channels at low pressures works against the technique. However, a miniaturized ion pump holds significant promise for meeting UHV requirements. The primary challenge for miniaturized ion pumps is electron trapping in a small volume at ultra-high vacuum in a manner that favors electron-gas collisions and suppresses electron-wall collisions.

In general, miniaturized ion pumps utilize a Penning cell structure similar to that used in commercial macro-scale ion pumps. The Penning cell structure consists of three electrodes (an anode and two cathodes) and a magnet. Planar titanium cathodes are sandwiched at the ends of a cylindrical-shaped anode and separated by a certain distance. The magnetic field is directed along the axis of the cylinder. Free electrons are produced from the cathodes by applying high electrical field between the anode and cathodes, and are confined to move in long spiral trajectories inside the cylindrical-shaped anode under the influence of crossed electrical and magnetic fields. Background gases are ionized by high kinetic energy electrons. Ions are accelerated toward the titanium cathode with sufficient energy to sputter fresh titanium molecules. The reactive background gas molecules (oxygen and nitrogen for example) are chemically absorbed by gettering action of exposed titanium; inert gas molecules (such as helium and argon) are ionized and implanted in cathode [Aud87, Sak94, Wel01]. One of our previous micro sputter-ion pump efforts utilized thin-film planar titanium electrodes at electrode gaps smaller than $150\ \mu\text{m}$, and successfully removed 168 Torr from a $6.33\ \text{cm}^3$ package at near-atmospheric pressures. In contrast to macro-scale ion pumps that work in high vacuum level ($<1\ \mu\text{Torr}$), no magnet is used in this ion pump, because magnet-less discharges can exist at higher pressure (close to atmospheric pressure) due to the mean-free path being close to the discharge gap at these pressures [Wri07]. Another of our previous efforts utilized a chip-scale Penning cell for sputter-ion pumping at operating pressure as low as $1.5\ \mu\text{Torr}$ in a $2.5\ \text{cm}^3$ package. This pump reduced pressure to <10 milliTorr from a starting pressure of 115 milliTorr in ≈ 4 hours of operation with 450-600 V applied across the device, and a 100-250 mW power consumption [Gre13].

In order to utilize a miniaturized ion pump effectively as an active pumping solution for atomic microsystems, however, a number of challenges still need to be addressed, ranging from ionization inefficiencies at high and ultra-high vacuum levels (<1 milliTorr), sensitivity of the atomic microsystem to magnetic fields, and effective noble gas pumping techniques.

Ionization inefficiencies at high vacuum levels: Mean free paths for electrons and gas molecules at nanoTorr pressure levels are typically on the order of 100 km. There are 30 - 300 million gas molecules in a volume of 1 cubic centimeter at these pressures. Both of these facts contribute to the dominance of gas-to-surface interactions in this pressure regime for miniaturized pumps. Ionization of the gas in miniaturized pumps would require either a very high rate of electron emission or very long-lived electrons. High rates of electron emission are possible to achieve with field emission arrays with surfaces that are covered with sharp tips capable of field ionizing any incident gas molecules [Gom94, Vel10]. Long-lived electrons can be achieved with structures such as Penning cell array that trap electrons in long orbits with the Lorentz

forces that arise from electric and magnetic fields [Gre13]. An RF electron trapping approach that does not use magnetic fields has potential for meeting this challenge, as this is an alternative way to trap an electron and elongate its trajectory to enhance ionization efficiency at high vacuum levels.

Sensitivity of the atomic microsystem to magnetic fields: Atomic inertial sensors are affected by magnetic fields, as these alter the relaxation process of the atoms during the relaxation period and thus the final atomic state that is measured is contaminated by information unrelated to the size of the inertial field. For instance, in NMRGs, changes of ~ 100 fT in the static field applied during measurement can result in an apparent change of the measured rotation rate of $1^\circ/\text{hr}$ [Kit11]. The Penning cell configuration widely used in macro-scale pumps and adapted for use in the reported micro sputter-ion pump is not ideal for atomic microsystems due to the size of the magnetic fields required for electron trapping and the challenges associated with shielding such fields and minimizing field gradients [Gre13]. In fact, the proposed RF electron trapping ion pump is a magnet-less approach toward this challenge. It does not require permanent magnets of any kind and only generates very small magnetic fields associated with electron and ion current.

Effective noble gas pumping techniques: A cesium resonance cell is implemented in recent chip-scale atomic clocks to provide a frequency standard [Lut04]. Transparent glass windows are anodically bonded to a silicon cavity to form the vacuum sealed cesium cell at 1 μTorr to enable laser interrogation of gaseous atoms in atomic clock systems [Lie04]. However, helium can easily diffuse through glass into the vacuum sealed cell driven by a concentration difference; this diffusion degrades the cell performance. Noble gases like helium are more difficult to pump because the gettering action of the pump does not assist; pumping is due to only ion and molecule burial. Macro-scale sputter ion pumps use alternative electrode architectures to improve noble gas pumping (e.g., “triode” or “slotted cathode” configurations). Thus, it is worthwhile to study the “triode” configuration in a miniaturized ion pump to enhance noble gas pumping.

Motivated by these needs, a new miniaturized magnet-less RF electron trap for a helium ion pump is described in this report. This work is divided into two tasks – experimental demonstration of the proof of concept, and numerical modeling of the electron trapping, ionization, and gas species burial. The design and experimental work described in this report involves two generations of the proposed electron trap. The modeling described here studies the parametric effects of gas pressure, electron energy, electron beam current, RF frequency, and RF voltage on the trapped electron density and ionization rates within the first generation device geometry.

1.2 Concept

In this work, the proposed architecture utilizes stacked micromachined elements, RF electron trapping, and a triode configuration to result in a miniaturized ion pump ($\sim 1 \text{ cm}^3$) capable of magnet-less ionization and pumping of noble gases – especially helium – at low pressures (~ 1 nanoTorr) and relatively low voltages (500 V). The pump configuration is shown conceptually in Fig. 1.

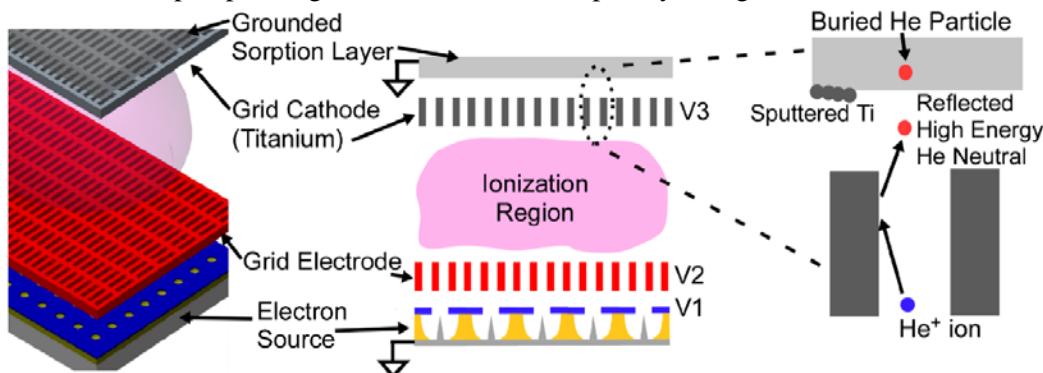


Fig. 1: Miniaturized ion pump concept: 3D model (left), 2D schematic (center), detailed view of grid cathode (right). The electron source (commercially available electron gun system or integrated field emitter array) provides electrons, which are trapped in the ionization region by an RF voltage between the grid electrode and grid cathode. The electrons ionize gas molecules, which are then accelerated into the grid cathode via a pulsed negative voltage. The ions collide with the cathode at shallow angles, and are reflected as neutral particles buried in the sorption layer backing the grid cathode. The titanium cathode is also sputtered by this action, which further buries the neutrals and getters active molecules from the environment.

1.2.1 Pump operation

There are three consecutive stages in this miniaturized helium ion pump: electron generation stage, electron trapping and helium ionization stage, and sorption stage. The electron generation, entrapment, and gas ionization occur in the first phase of operation, during which RF power is applied. Following this, the RF power is switched off and the ions are accelerated toward the sorption layer by a DC voltage.

Electrons can be generated by a commercially available electron gun system or an integrated field emitter array. The generated electrons are then trapped between two grid electrodes via application of an RF voltage. The electrons are oscillated in this region, and the extended trajectory and kinetic energy are sufficient for ionizing the target gas. Ions build up in the ionization region while the RF voltage is applied, as the high frequency electric fields do not tend to appreciably accelerate the relatively massive ions. After sufficient ionization time, the RF voltage is switched off, and the ions are accelerated into the grid cathode (and away from the electron source) using a DC voltage. The ions collide with the surfaces of the cathode at shallow angles. This collision angle results in neutralization and reflection of the ions, and the now neutral particles continue on their reflected trajectory unaffected by electric fields. The high energy neutral particles are buried into the sorption layer. Neutralizing and reflecting these particles away from the grid cathode and into the sorption layer results in a lower likelihood of later re-release through continued sputtering action of the grid cathode. The grid cathode is to be made from a sputterable getter (titanium); the sputtering action of any heavy ions bombarding the cathode will not only further bury neutral particles but also will result in titanium gettering of reactive molecules (oxygen, nitrogen, hydrogen) that may be present in the pump chamber. Importantly, the cathode is to be biased at a negative voltage with respect to the sorption layer and the base of the electron source during ion acceleration; this results in ions being attracted only to the cathode and away from both the electron source and the gas particles buried in the sorption layer.

There are several specific innovations in this concept, which have not been previously investigated at a miniaturized scale:

- (i) Gas ionization with electrons with trajectories lengthened via RF voltage (magnets not required);
- (ii) Slotted/grid cathode for generating and burying high energy neutrals for enhanced noble gas pumping;
- (iii) Sputterable titanium cathode for pumping of reactive gases that may be desorbed during pump startup or due to thermal transients;
- (iv) “Triode” configuration for protecting pump elements during ion sorption and avoiding release of buried gas particles;
- (v) Integrated magnet-less ion gage for low dead volume in situ pressure measurement.

1.2.2 Pump architecture

Electron trapping and helium ionization

Generated electrons will pass through the grid electrode and into the ionization region. With no further electric field manipulation and at nanoTorr pressures, there would be an extremely small probability of interaction of these electrons with any gas molecules present in the ionization region, as the mean free path of electrons at 1 nanoTorr pressure (3.5×10^7 molecules/cm³) of helium (140 pm diameter) is approximately 330 km. The fraction of electrons that have not collided with a gas molecule, ϕ , after traveling a distance x is related to the mean free path λ as given by [Lie94]:

$$\phi = e^{-x/\lambda} \quad (1)$$

In a millimeter scale cavity, >99.9995% of electrons would not collide with a helium molecule before being lost to the pump surfaces. This very small probability of collision could be overcome by flooding the ionization region with electrons, but this implies high currents and associated high power and high temperature in the electron source. Instead, we will improve ionization efficiency by trapping the electrons in the ionization region via application of RF voltage V_{RF} between the grid electrode (V2) and the grid cathode (V3) as shown in Fig. 1. If the voltage is cycled at a high enough RF frequency f_{RF} , the electrons will oscillate indefinitely between the two grids – or until a collision occurs. Based on the Lorentz force

on an electron, the minimum f_{RF} that will limit the full length of the electron excursion to d , the gap between the electrodes, is:

$$f_{RF} \geq \sqrt{\frac{q|V_{RF}|}{2\pi^2 m_e d^2}} \quad (2)$$

where q is the fundamental charge, m_e is the mass of the electron, and $|V_{RF}|$ is the amplitude of the RF voltage applied between the grid electrode and the grid cathode. As a representative case, a voltage amplitude $|V_{RF}|$ of 200 V and a gap d of 5 mm would require a minimum frequency f_{RF} of 240 MHz to trap the electrons. At this frequency or slightly higher, the electrons would travel 750 km in 300 ms. According to (1), this is a sufficient distance to ensure that better than 60% of the electrons collide with a gas molecule. Not every collision is an ionizing collision, however. The electron-ionization cross section σ_{iz} for helium at the average (RMS) kinetic energy of 141 eV in this case is approximately $4 \times 10^{-21} \text{ m}^2$ [Pan90]. At a pressure of 1 nanoTorr and with the average velocity of the electrons in this case, approximately 0.74 ionizing collisions per second per electron are expected, as calculated by [Lie94]:

$$\nu = n\sigma_{iz}v \quad (3)$$

where ν is the ionization rate per electron, n is the number of gas molecules per unit volume, and v is the average electron velocity ($5.33 \times 10^6 \text{ m/s}$ for the current example). In order to pump at the desired 1 mL-nanoTorr/s ($3.5 \times 10^7 \text{ molecules/s}$), each helium molecule to be pumped must be ionized and thus at least $4.7 \times 10^7 \text{ electrons/s}$ (the equivalent of 7.5 pA) must be trapped in the ionization region. If the duty cycle of the RF applied power is less than 100%, then the electron current required from the electron source is higher in inverse proportion.

Sputterable grid cathode and sorption layer

After a period of RF electron trapping and ionization, the pump will cycle into a sorption mode to remove the ionized gas. The proposed sputterable grid cathode and sorption layer will accommodate the pumping of both helium and water vapor (which may be present from plasma-induced or thermally-induced surface desorption). When the sorption mode begins, the RF power is switched off, and the ions will then be accelerated toward the grid cathode via application of a DC voltage V_3 that is negative (-100 to -400 V) with respect to the grounded pump walls. Note that this is a pulsed DC voltage, and not on during the electron trapping phase of the pumping. This is a “Triode” configuration that will protect the electron source from ion bombardment. Helium pumping will be enhanced by the grid cathode (Fig. 1.2), which provides an array of vertical facets that are almost parallel with the incoming ion trajectories. When ions collide with these surfaces at shallow angles, the ions are neutralized and reflected. The resulting high energy neutrals continue on their reflected trajectories – unaffected by electric fields – and are buried at the grounded sorption layer. This configuration results in the burial of helium molecules at locations that are not further bombarded by ions, ensuring that the buried helium molecules are not later released through continued pump operation (plasma-induced desorption or sputtering). Water vapor pumping will be accomplished via the sputtering action of the patterned titanium cathode, with the sputtered titanium chemically reacting with the water vapor constituents and removing them from the ambient. Any sputtering action and subsequent deposition on the nearby sorption layer will also further bury the neutral gas molecules implanted there. At the applied voltages and corresponding ion/neutral energies, it is likely that helium will be very shallowly implanted in the sorption layer ($<100 \text{ \AA}$, as for low energy ($<600 \text{ eV}$) helium ions implanted in tungsten [Gor80]), while later diffusing into the sorption layer. Sputtering yield for a titanium target via low energy ($<1 \text{ keV}$) helium ions is expected to be <0.1 [Ros62]. Thus, when only helium is being pumped, the voltage applied to accelerate the ions will be made as small as possible while still resulting in shallow implantation. If sputtering is required to pump larger species than helium, the accelerating voltage may need to be at least -400 V.

2.0 Significant accomplishments in Phase I

- RF electron trapping has been demonstrated experimentally and with numerical Hybrid Plasma Equipment Modeling.
- Low power resonant RF operation has been experimentally demonstrated. An equivalent circuit model and a simplified trapping model for the first generation electron trapping module has been developed, allowing the optimal operating parameters (frequency, power) to be estimated and used for demonstration.
- The Hybrid Plasma Equipment Modeling code has been developed to allow RF frequencies and low pressures. This model has been utilized to numerically validate 100x performance improvement in ionization rates with RF electron trapping versus DC electron impact ionization.
- Ionization rate measurement techniques have been devised and investigated, with many lessons learned for future work.
- A second generation enhanced efficiency electron trap module has been designed, fabricated, and assembled. Key features include ultra-fine perforated electrodes for improved electric field uniformity, a sorption layer to enable pumping demonstration, and much-improved volume utilization compared to the first generation device. Characterization of this second generation is forthcoming.

3.0 Task by task account of progress

3.A Task A – Experimental proof of concept

- Task A Objectives
 - Simple component-level modeling and design:
 - Electrostatic modeling
 - Pump conductance versus pump dead volume
 - Grid geometry and electrode gaps
 - Fabrication and assembly of experimental devices
 - Establishment of an appropriate RF vacuum test chamber
 - Characterization of electron trapping and ionization rates from first generation devices
 - Design of improved second generation devices
 - Fabrication and assembly of second generation devices
- Task A Accomplishments

3.A.1 – Analytical model of RF electron trapping concept

A simple analytical model for demonstrating the RF electron trapping concept is depicted in Fig. 2. Two parallel electrodes, RFA and RFB, are separated by a gap, d . In order to trap and oscillate the electrons in between RFA and RFB electrodes, a RF voltage V_{RF} is applied at RFA and cycled at frequency f_{RF} , while RFB is grounded to limit the x-axis electron excursion within $\pm d/2$, half of the gap between the parallel electrodes.

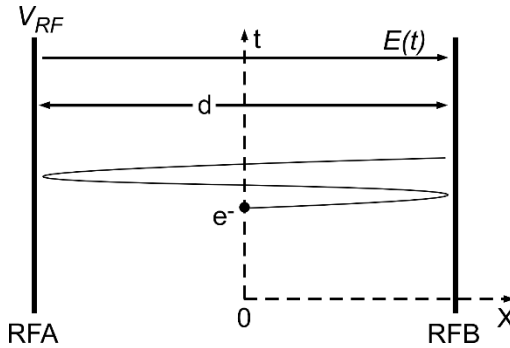


Fig. 2: Analytical model of RF electron trapping. V_{RF} is the RF voltage applied between two RF electrodes at RF frequency f_{RF} , while $E(t)$ indicates the associated electric field.

Based on the Lorentz force on an electron, equation 2 was derived to show the relationship between the magnitude of the applied RF voltage $|V_{RF}|$, RF frequency f_{RF} , and electrode gap d for an established RF electron trap. For a given f_{RF} and d , there is a perfect RF trapping voltage $|V_{RF_perfect}|$ that can enable the electrons to travel the entire electrode gap during a RF cycle. From equation 2:

$$|V_{RF_perfect}| = (2\pi f_{RF})^2 \frac{m_e d^2}{2q} \quad (4)$$

By extending the trajectory of the electrons to the full extent of the trapping region, the total distance traveled per cycle is maximized. If the RF voltage $|V_{RF}|$ exceeds this value, electrons are accelerated into the electrodes before turning back. At lower values of RF voltage, the electron trajectory and effective trap volume are diminished, reducing the acceleration time as well as the likelihood of interaction with gas molecules. Therefore, a trapping efficiency factor k_f associated with RF frequency is introduced into equation 4 to fully describe any established RF electron trap:

$$|V_{RF}| = \left(\frac{2\pi f_{RF}}{k_f} \right)^2 \frac{m_e d^2}{2q} \quad (5)$$

For a given RF frequency f_{RF} and gap d , $k_f = 1$ represents the most desirable value, with gradual losses in performance as k_f deviates from this value. As a representative case for d of 5 mm and f_{RF} of 240 MHz, the perfect RF trapping voltage $|V_{RF_perfect}|$ is 200 V.

3.A.2 – Electron trapping module (ETM) design and fabrication

There are several architectural and material considerations in designing the electron trapping module (ETM) to prove the concept of RF electron trapping.

Stacked and reconfigurable architecture (Fig. 3, Fig. 4(a)): This architecture provides flexibility in layer thickness and composition that can be achieved by simply stacking multiple layers together through two alignment holes in each layer. All layers other than two perforated RF electrodes (RFA and RFB, Fig. 4(c)) possess the same U-shaped topography with a 1 cm x 1 cm opening area; this permits the incoming electron into the trap formed between RFA and RFB, and controls the cross-sectional area of the overall trapping region. Meanwhile, RFA and RFB are separated by the U-shaped chassis (Fig. 4(d)), the thickness of which controls the dimension d of the trap. Additional U-shaped metal layers can be easily accommodated into the ETM to provide additional electrical biasing; these are labeled as biasing metal plates A and B in Fig. 3. These can be used to, for instance, alter the electron beam energy or alter the electric field near RFA and RFB. The electrical connection to a metal layer is realized by a short extension past the edge of the electrode. The through-hole in the extension provides a bolted connection point to ultra-high vacuum grade solid core wire, which then connects to the electrical feedthrough in the vacuum chamber. All extensions are offset from each other for accessibility during assembly. U-shaped ceramic sheets (Fig. 4(b)) between different metal layers provide electrical isolation between metal layers. This reconfigurable configuration maximizes the potential for quick prototyping to explore the parameter space. For example, the gap between two perforated stainless steel RF electrodes can be simply changed by swapping the U-shaped stainless steel chassis with a chassis of a different thickness. Also, many perforated stainless steel RF electrodes can be stacked to alter the aspect ratio of the perforations.

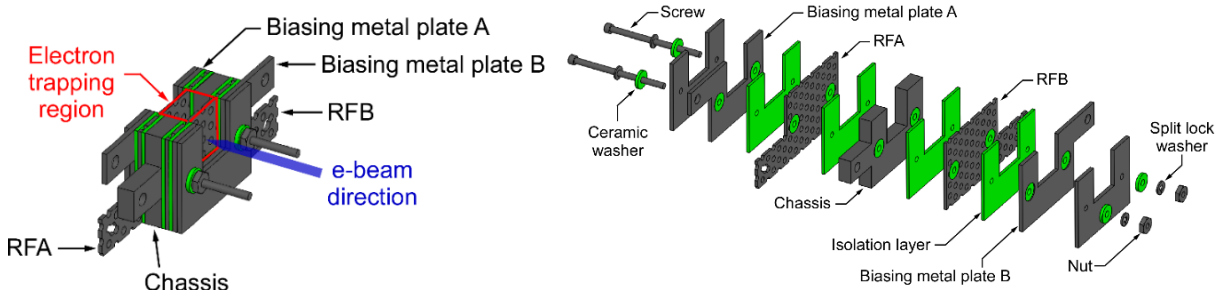


Fig. 3: Schematic and exploded view of electron trapping module (ETM).

Electrode materials: The testing environment of ETM is in the sub- μ Torr vacuum level, thus, all metal electrodes as well as the insulation layers should have low outgassing rate to minimize the gas load, and the ability to withstand baking at temperature as high as 300 °C for the final sub-nanoTorr operation. In addition, all metal must be non-magnetic or soft magnetic material to ensure the non-magnetic trapping environment. Candidate materials include aluminum and non-magnetic stainless steels such as annealed 304 stainless steel.

Insulation materials: The RF electron trapping of helium requires a relatively high RF electric potential in between the two perforated RF electrodes to establish the trap, and the resulting electric fields will also be relatively large because of the miniaturization of the device. Thus, the insulation layers are fabricated from superior insulating materials. Ceramic, and especially machinable ceramic (Macor), is particularly suitable for these requirements.

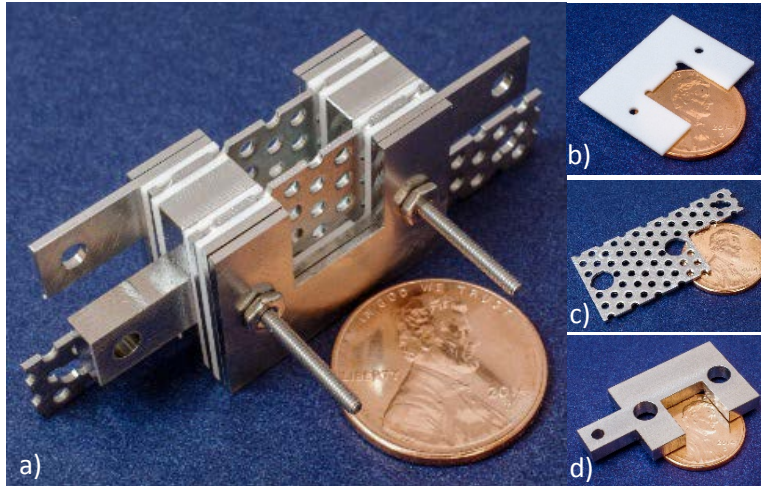


Fig. 4: a) The ETM consists of two perforated stainless steel RF electrodes, separated by a U-shaped stainless steel chassis with two U-shaped ceramic sheets for electrical isolation. b) U-shaped ceramic sheet. c) Perforated stainless steel RF electrode. d) U-shaped stainless steel chassis.

The two perforated RF electrodes are machined from 0.762 mm thick 304 stainless steel sheet patterned with 1.5875 mm diameter staggered holes. Those reported here have 40 mm length and 19 mm width when also considering the length of the extension. The two RF electrodes are machined such that the perforation patterns are well-aligned once they are stacked. The U-shaped ceramic layers (25.4 mm x 19 mm) are machined from 0.75 mm thick machinable ceramic Macor sheets, and two 1.695 mm diameter alignment holes are drilled. For this particular ETM, the U-shaped chassis is also made from a 304 stainless steel sheet, and trimmed down to 5.5 mm in thickness.

3.A.3 – Vacuum test setup

A schematic of the vacuum setup is shown in Fig. 5. This system provides the vacuum environment for the RF electron trapping testing. An all-in-one turbo pump (Agilent, Mini-TASK AG81), capable of pumping down to <100 nanoTorr, and a sputter ion pump (Agilent, 20 L/s VacIon Pump), capable of pumping down to 0.1 nanoTorr, are connected to the vacuum chamber (Kimball Physics, 2.75" Double Spherical Cube Vacuum Chamber) through a tee connector. The two pumps can be isolated from the vacuum chamber separately via manual control of the associated isolation valves. One vent valve (Kurt J. Lesker, 2.75" CF Manual Bellows Sealed SS Angle Valves) is also attached to the miniaturized chamber for venting the vacuum. Helium can be precisely leaked into the chamber with the leak valve (Agilent, Variable Leak Valve). The pressure inside the chamber can be continuously monitored by the ion gauge (Adixen, AHC 2010). One BNC electrical feedthrough (Kurt. J Lesker, 2.75" CF 4xBNC) and another SHV electrical feedthrough (Kurt. J Lesker, 2.75" CF 4xSHV) are assembled to the chamber to provide electrical accesses to all metal layers of the ETM. An electron gun (Kimball Physics, FRA-2X1-2 Electron Gun) with an insertion length of 150 mm provides the electron source for the RF electron trapping testing. The electron gun is offset with a custom 2.75" CF full nipple by 58.74 mm from the right side of the chamber, such that the tip of the cathode barrel for the electron gun is only 10.7 mm away from the RFB surface in the ETM. This separation is close to the limit of working distance for this electron gun, and maximizes the electrons being shooting toward the trapping region. In addition, several customized stands are made to not only mechanically support the setup, but also adjust the vertical position of the different components.

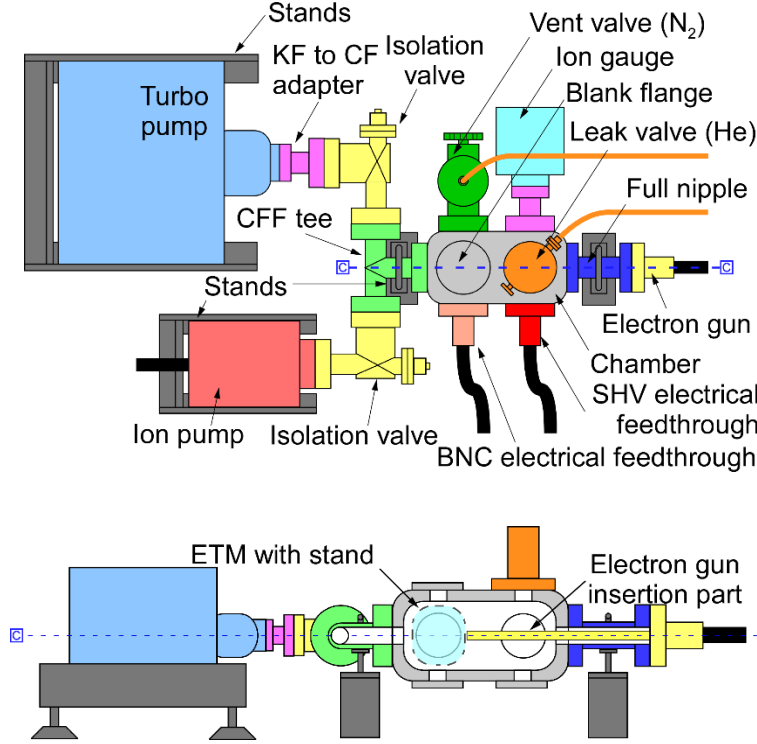


Fig. 5: The vacuum setup consists of a commercial combination diaphragm/turbo pump (Agilent Mini-TASK AG81) and a commercial sputter ion pump (Agilent, 20L/s Valcon Pump) capable of pumping down/to pump down to 10 nanoTorr. The two isolation valves can separately isolate the pumps from the chamber. Two electrical feedthroughs provide electrical connection to the ETM, where it is placed inside the left part of the chamber. The electron gun is also attached to the chamber, with the barrel tip 10.7 mm from the ETM. A leak valve can precisely control the leakage of helium into the chamber. The ion gauge (Adixen, AHC 2010) continuously monitors the pressure inside the chamber.

The ETM, along with a customized ceramic stand (Fig. 6(a)), is placed in the left part of the chamber close to the BNC electrical feedthrough. The ceramic stand is machined from a machinable Macor bar, and fixed on top of the blank flange – located on the left bottom side of the chamber – by two 2.75" Groove Grabbers (Kimball Physics, MCF275-GrvGrb-C02). This stand provides electrical isolation between the ETM and the grounded chamber. The ETM is tightly fixed on top of the ceramic stand, with the trap opening perpendicular to and centered on the tip of the electron gun barrel. The blue arrow in Fig. 6 indicates the incoming direction of the electron beam. In order to effectively prove the proposed RF electron trapping concept, two additional collectors are added into the testing setup. Collector 1 covers the top of trapping region, and is bolted together with other layers from the back end of ETM. Collector 2 is clamped to the ceramic stand, and is located opposite to the electron gun barrel, on the back of ETM. In addition, a perforated Cutoff electrode is stacked with other layers and bolted onto the ETM. The perforation patterns of all three perforated electrodes (RFA, RFB, and Cutoff) are well aligned to ensure incoming electrons can pass into the trap. The Cutoff electrode is the perforated electrode closest to the electron gun, so it can prevent the electrons from going into the trap if it is biased to a positive potential.

The RFA, RFB, and Cutoff electrodes and the Chassis are closest to the trapping region. For these, BNC electrical feedthroughs are used to reduce the parasitic inductances and capacitances for the RF electron trapping testing. The two collectors (Collector 1 and Collector 2) and the two biasing metal plates (Biasing metal plate A and Biasing metal plate B) are electrically connected to the SHV electrical feedthrough via solid core wire. This feedthrough can accommodate high voltage (>1 kV) DC and pulsed DC signals.

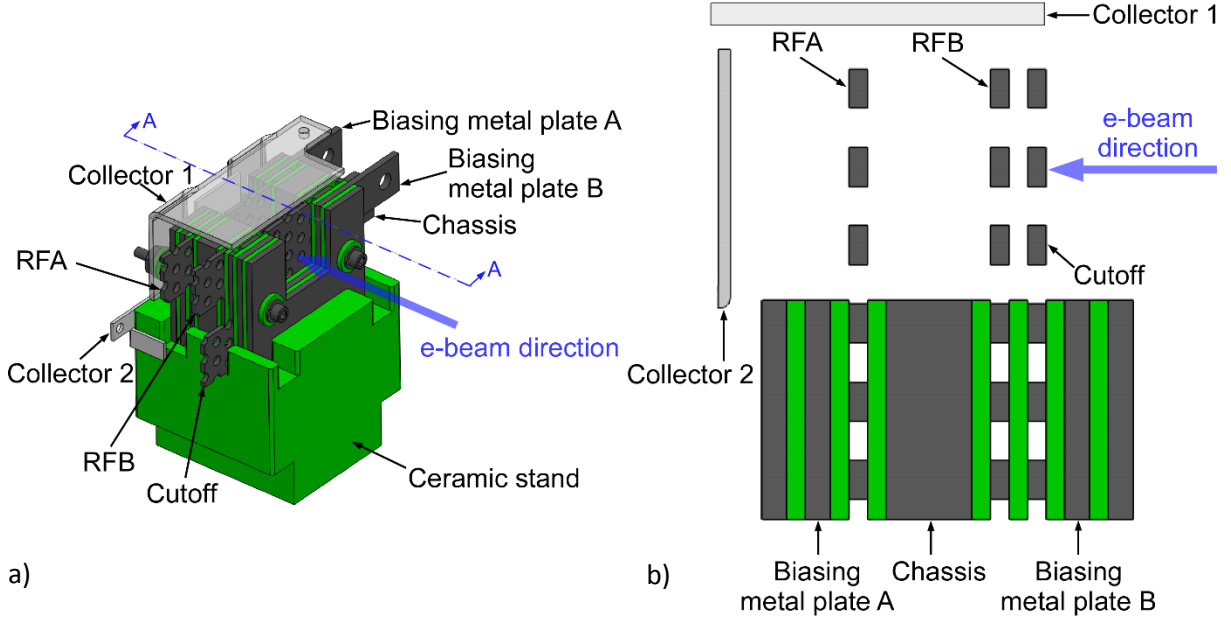


Fig. 6: Testing setup. a) The ETM is electrically isolated and fixed in position within the chamber by a ceramic stand. The electron beam is directed into the ETM with its spot size (20 mm) covering the exposed perforated electrode. Two collector electrodes cover both the top and back side of the trap, and are used in diagnostic measurements. b) A-A cross sectional view of the ETM with two collector electrodes.

3.A.4 – ETM RF characterization and modeling

Once the ETM is fixed inside the vacuum chamber, all electrodes and the chamber are grounded to the same ground except RFA, where the RF voltage is applied. The impedance analyzer (Agilent 4395A) is calibrated with three calibration standards (short, open, and load) from 20 MHz to 300 MHz before impedance measurement. Then, a 30 cm long LMR-400 low loss RF coax cable is connected between RFA via the associated BNC electrical feedthrough and the impedance analyzer. The impedance of the ETM along with the cable is measured in the calibrated frequency range via the impedance analyzer. Because experimentally measured impedance results are affected by the presence of the transmission line (coaxial cable), the ETM impedance Z_L (Fig. 7) can be de-embedded from measured impedance result by shifting the reference plane to RFA by utilizing a lossless cable assumption and a lossless transmission line equation [Qia09]:

$$Z_{in}(f) = Z_0 \frac{Z_L + jZ_0 \tan\left(\frac{2\pi f}{k_v c}\right)}{Z_0 + jZ_L \tan\left(\frac{2\pi f}{k_v c}\right)} \quad (6)$$

where Z_{in} is the impedance measured along with the coax cable, Z_0 is the characteristic impedance (50 Ω), f is the frequency, c is the speed of light, and k_v is the velocity factor of cable being used (0.85 for LMR-400).

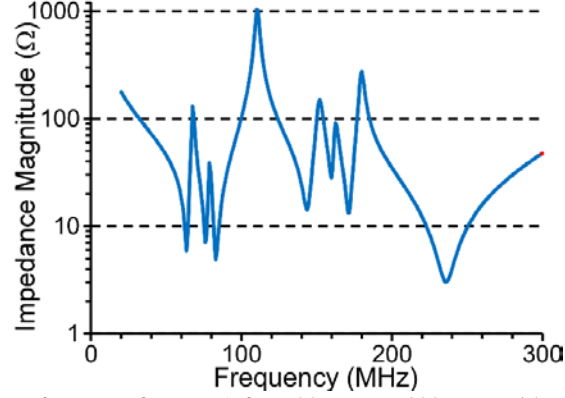


Fig. 7: The de-embedded impedance of ETM Z_L from RFA from 20 MHz to 300 MHz with all electrodes except RFA grounded.

The de-embedded impedance (Fig. 7) shows seven resonant dips, with each dip indicating a series resonance formed between RFA and the seven other electrodes in the ETM. Therefore, a simplified equivalent circuit model (Fig. 8) with seven series RLC branches in parallel is developed to represent the ETM. Taking a look at the RFB branch of the equivalent circuit model, for example, a capacitor C_{RFB} is formed between the RF electrodes. However, a stray resistance R_{RFB} and a stray inductance L_{RFB} are also presented due to the unshielded wires in the vacuum chamber, the contact resistances of these wires, and the skin effect within the electrodes. These parasitic components along with the capacitance cause a series resonant dip in the device impedance. Because electrons will be trapped between RFA and RFB electrodes during RF electron trapping testing, the generated RF electron trap can be well-represented electrically with C_{RFB} in the developed circuit model. In this way, the RF voltage developed across the trap during RF electron trapping testing with a given input power and frequency can be estimated by calculating the developed voltage across C_{RFB} in the equivalent circuit model. Meanwhile, the effect of the operating RF frequency f_{RF} and output RF power P_{out} on the electron trapping efficiency can be explored by combining the equivalent circuit model with the analytical model developed in Section 3.A.1.

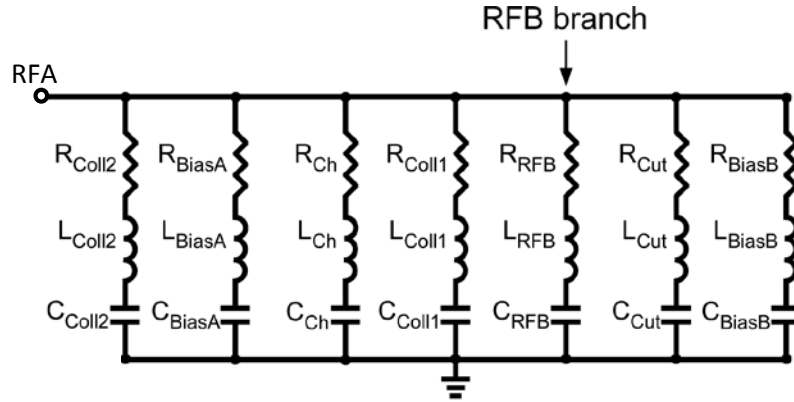


Fig. 8: The equivalent circuit model of ETM. The de-embedded device impedance results (Fig. 7) suggest that the seven electrodes in the device (aside from the driven RFA electrode) form parallel resonant branches, and each branch also has a series resonant behavior.

In order to assign the series resonant frequencies in the de-embedded impedance in Fig. 7 to the correct branches of the equivalent circuit model, an experimental method is developed in which only one branch is loaded with an inductor (225 nH) between the electrode of that branch and ground, and identifying shifts of the series resonant dips in the measured (de-embedded) impedance. For example, by loading an inductor (225 nH) in between Collector 1 and ground, only one series resonant dip that originally is at 160 MHz when Collector 1 is grounded (blue impedance trace in Fig. 9) is shifted to 95 MHz (red impedance trace in Fig. 9), so the series resonant frequency associated with the Collector 1 branch is 160 MHz. In this way,

the series resonant frequencies of all seven branches can be identified. This results in the knowledge of the fixed ratio between the capacitance and inductance in each branch. The approximate stray resistance in each branch is also determined in this way, as the device impedance at the series resonant frequency of that branch is dominated by the resistance in that branch.

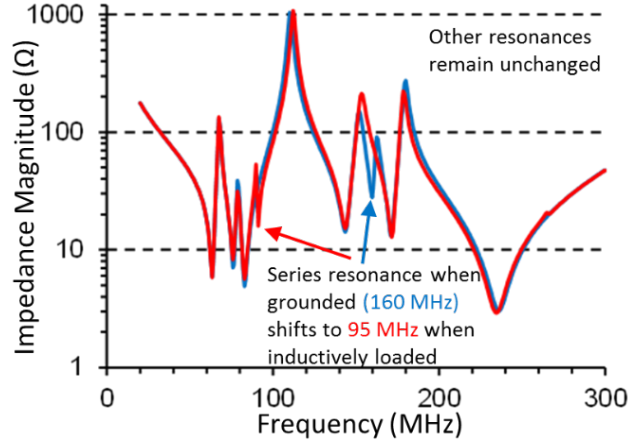


Fig. 9: The series resonance associated with each branch in the circuit is determined experimentally by loading one branch with an inductor (225 nH), and identifying the shift in the measured impedance spectrum. For example, loading the Collector 1 branch shifts the series resonance at 160 MHz to 95 MHz, while other series resonances are unaffected.

The capacitances from RFA to every other electrode are first measured with a LCR meter (Hewlett-Packard 4284A precision LCR meter). This provides a rough estimation for capacitance value in series RLC branches. The inductance in each series RLC branch is estimated using the measured capacitance and the series resonant frequency associated with that branch. Simulations are then performed in SPICE, tuning all of the inductances and capacitances to match not only the series resonant dips, but also the parallel resonant peaks in the de-embedded device impedance results. From the result in Fig. 10, the SPICE simulated impedance of the ETM (red impedance trace) is well matched to the de-embedded ETM impedance as shown in blue impedance trace. This indicates that the equivalent circuit model is an appropriate representation of the ETM, so the actual RF voltage dropped across the two RF electrodes in the ETM can be estimated with the voltage developed on C_{RFB} . The values of all components in the equivalent circuit model are summarized in Table 1.

Table 1: Summary of series resonant frequencies, capacitances, inductances, and resistances of seven branches in the equivalent circuit model.

Branch	Series resonant frequency f (MHz)	Resistance R (Ω)	Inductance L (nH)	Capacitance C (pF)
Chassis	63.3	6.25	1210.00	5.23
Cutoff	75.9	6.25	916.90	4.80
Biasing metal plate A	82.8	6.25	400.10	9.23
RFB	143.6	18.75	921.25	1.33
Collector 1	159.7	28.12	3103.75	0.32
Collector 2	171.5	15.63	747.50	1.15
Biasing metal plate B	235.8	3.44	47.44	9.60

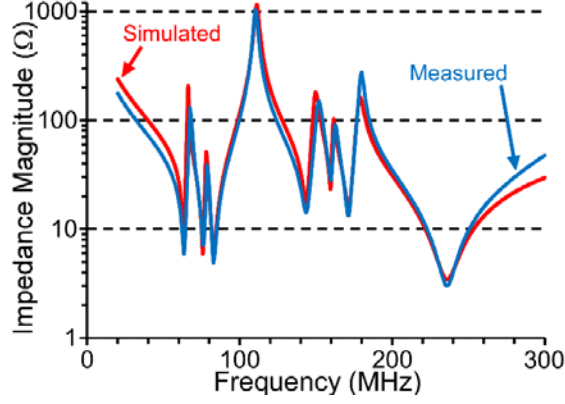


Fig. 10: The SPICE simulated ETM impedance magnitude (red curve) compared with the de-embedded ETM impedance magnitude (blue curve).

The equivalent circuit model allows calculation of the amplitude of the RF voltage $|V_{RF}|$ developed across the C_{RFB} for given output RF power levels P_{out} from the signal generator. First, the voltage reflection coefficient Γ is calculated to derive the amount of power being delivered to the ETM, P_{Fwd} :

$$\Gamma = \frac{Z_L - Z_0}{Z_L + Z_0} \quad (7)$$

$$P_{Fwd} = P_{out} \cdot (1 - |\Gamma|^2) \quad (8)$$

where Z_L is the device impedance (complex) from the de-embedded impedance result of ETM, and Z_0 is the characteristic impedance of the source and transmission line (50 Ω). For example, the amount of power absorbed by the ETM P_{Fwd} is 31% of output RF power P_{out} at RF frequency f_{RF} of 143.6 MHz. Then, the peak voltage across the ETM $V_{L,peak}$ can be calculated and, from this value, the peak current through the RFB branch $I_{RFB,peak}$ can be calculated:

$$P_{Fwd} = \frac{V_{L,peak}^2}{2Z_L} \rightarrow V_{L,peak} = \sqrt{2P_{Fwd} \cdot Z_L} \quad (9)$$

$$I_{RFB,peak} = \frac{V_{L,peak}}{R_{RFB} + j\left(\omega L_{RFB} - \frac{1}{\omega C_{RFB}}\right)} \quad (10)$$

The amplitude of the RF voltage $|V_{RF}|$ across C_{RFB} follows as:

$$|V_{RF}| = \frac{|I_{RFB,peak}|}{\omega C_{RFB}} = \frac{\sqrt{2P_{out} \cdot \left(1 - \left|\frac{Z_L - Z_0}{Z_L + Z_0}\right|^2\right) \cdot Z_L}}{\left|R_{RFB} + j\left(\omega L_{RFB} - \frac{1}{\omega C_{RFB}}\right)\right|} \cdot \frac{1}{\omega C_{RFB}} \quad (11)$$

By substituting the values of components identified in the equivalent circuit model and the measured de-embedded device impedance in equation 11, the amplitude of RF voltage $|V_{RF}|$ developed at RFA is calculated over the frequency range at different output RF power levels P_{out} (three colored curves in Fig. 11). For any specific output RF power level, even without an RF matching network in between the RF source and the ETM, $|V_{RF}|$ is boosted and peaks at 143.6 MHz - the series resonant frequency in RFB branch - due to the resonant amplification of the series RLC circuit. From the power efficiency perspective, the lowest power to generate a given $|V_{RF}|$ at RFA will be achieved when the ETM is operated at the series resonant frequency of the RFB branch. Also, based on the analytical model of RF electron trapping, a trace indicating the perfect RF trapping voltage $|V_{RF,perfect}|$ (the trapping efficiency factor $k_f = 1$) for this specific 7 mm gap device over the frequency range is plotted in Fig. 11. As $|V_{RF}|$ becomes lower than the perfect RF trapping voltage for a given frequency ($k_f > 1$), the RF trapping is expected to exist but the efficiency is diminished, since reduced excursion of trapped electrons will result in a smaller effective RF electron trapping region. By substituting into equation 11 the calculated $|V_{RF,perfect}|$ associated with a

specific RF frequency f_{RF} derived in equation 4, the required output RF power to initiate this perfect RF electron trapping can be calculated. The calculated optimal operating RF signal for the 7 mm gap ETM is at RF frequency f_{RF} of 143.6 MHz, and an output RF power P_{out} of 0.836 W.

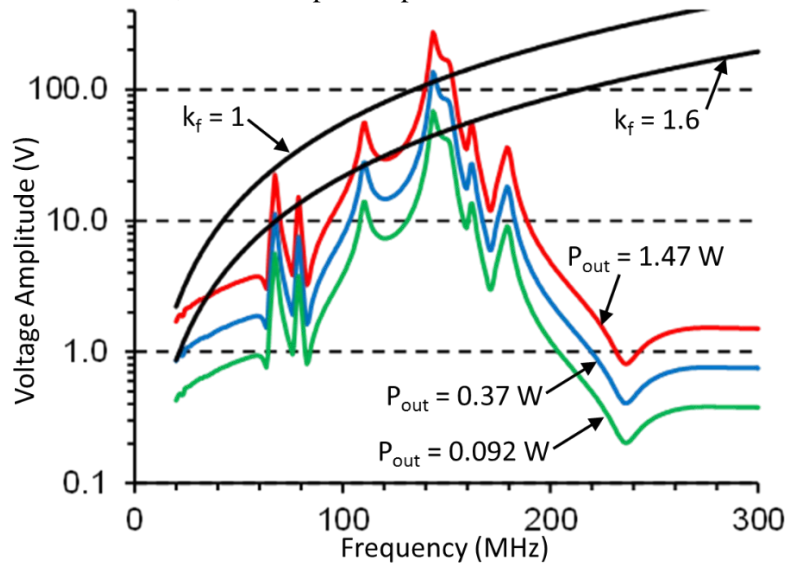


Fig. 11: Three colored curves indicate peak RF voltage $|V_{RF}|$ developed at RFA across the frequency range with different output RF power P_{out} . No electron trapping is expected to occur based on the analytical model, when peak RF voltage is higher than the perfect RF trapping voltage $|V_{RF_perfect}|$ as indicated by the $k_f = 1$ curve. A k_f greater than 1 is expected to result in electron trapping, although the excursion of the electron within the trap is reduced as k_f increases.

3.A.5 – ETM RF electron trapping characterization

For a typical capacitively coupled plasma (CCP) utilized in the commercial RIE chamber, a capacitor is usually placed in between the RF power source and a powered electrode. This electrode is isolated from the grounded chamber to store electrons and build up a negative DC bias voltage. This negative DC bias attracts positive ions across the plasma sheath to bombard, react with, and etch the substrate [Sug98]. Inspired by the CCP approach, a DC floating potential measurement scheme is developed for RF electron trapping testing. The DC blocking capacitors are added between electrodes and ground to DC float the electrodes, while still passing the AC RF signal during testing. In this way, the electrons that collide with the electrodes initially result in a negative potential at electrodes with DC blocking capacitors. Eventually, the floated electrodes became sufficiently biased to repel all the electrons, establishing a dynamic equilibrium state between the DC floating potential across the capacitors and the electron cloud in the trapping region. The magnitude of the negative floating potential is related to the electron density near the electrodes, as a higher electron density requires larger repelling force from the electrodes (and thus a more negative floating potential) to overcome the larger inter-electron repulsive forces.

The electrical testing setup to prove RF electron trapping is shown in Fig. 12. By putting DC blocking capacitors (86 pF) in series with electrodes near trapping region – RFA, Collector 1, and Chassis, while grounding all other electrodes, the value of DC floating potentials at Collector 1 and Chassis are an indication for electron density in the trapping region. A high impedance 10 to 1 ratio voltage divider is in parallel with DC blocking capacitor. Meanwhile, the DC floating potential is measured by attaching a digital multimeter (Agilent 34401A, Input impedance $> 10 \text{ G}\Omega$) in parallel with the $0.1 \text{ G}\Omega$ resistor in the voltage divider. Therefore, the overall $1.1 \text{ G}\Omega$ impedance is high enough to avoid establishing a significant leakage path for electrons. No major shifts in the impedance measurement of the ETM were found despite the presence of these capacitors. This is due to the capacitances of the DC blocking capacitors that are in series with the associated electrodes being much larger than the capacitances identified in the equivalent circuit model, thus not significantly changing the overall capacitance in each series RLC branch.

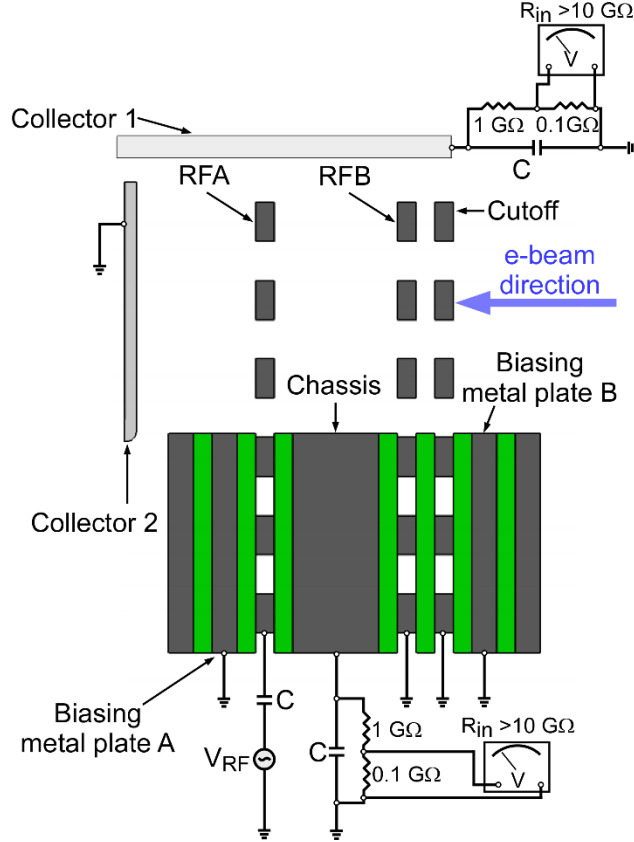


Fig. 12: Electrical testing setup for RF electron trapping. DC blocking (AC passing) capacitors are added to Chassis, and Collector 1 electrodes. Another capacitor is added between the RF source and the RFA electrode. The potential across Chassis and Collector 1 capacitors is measured with a high impedance voltage divider and voltmeter, minimizing the electron drain from the trap. A more negative potential across these capacitors is correlated with higher electron density near the associated electrode.

All RF electron trapping tests were done under same electron beam conditions of $40\ \mu\text{A}$ steady emission current and $15\ \text{eV}$ electron energy. Also, a $70\ \text{nanoTorr}$ vacuum level was maintained during all testing periods.

3.A.5.1 – Reference measurement of electron beam: The “steady state” floating potentials (SSFPs) across the DC blocking capacitors with only the presence of electron beam are recorded as a reference. As a note, it takes about two hours to warm up the electron gun until it reaches a stable emission state, then an additional half an hour is needed to allow the floating potentials across the DC blocking capacitors to arrive at “steady state”.

3.A.5.2 – Power variation measurements: The “steady state” floating potentials (SSFPs) at Collector 1 and Chassis are measured under different output RF power levels P_{out} at $143.6\ \text{MHz}$, which is the calculated optimal RF frequency f_{RF} to achieve the best power efficiency as identified from previous analytical models. Several P_{out} levels ranging from $0.105\ \text{W}$ to $1.668\ \text{W}$ are studied here. The optimal operating $P_{out} = 0.836\ \text{W}$, identified in section A.5, is covered in this range as well. First, 30 seconds before turning on the RF at a specific power level, a customized LabVIEW® data acquisition program is started to simultaneously record all voltage readouts from the digital multimeters during the course of the RF electron trapping testing. Once the RF is powered on, observable changes in both Collector 1 and Chassis floating potentials occur over a course of minutes. Eventually the two floating potentials arrive at a new stabilized “steady state” before the end of data acquisition. At this point, the measurement is concluded, the RF power is switched off, and the DC blocking capacitors are shorted with a $10\ \text{M}\Omega$ resistor to discharge any charge built up during RF electron trapping. Typically, a two hour wait after this process is required for the floating

potentials to return to “steady state” values with just the electron source. Then, a new RF power level is selected, and the experiment repeated.

3.A.5.3 – Frequency variation measurements: The SSFPs at Collector 1 and Chassis are measured at several RF frequencies f_{RF} between 141 MHz and 152.5 MHz at a fixed output RF power P_{out} of 0.836 W. This set of measurements also covered the optimal operating RF signal, f_{RF} of 143.6 MHz, and P_{out} of 0.836 W, derived from the foregoing measurements and models. The testing protocol is similar to that described in the *power variation measurements* section.

3.A.5.4 – Reference measurements of RF: In the absence of electron beam, the SSFPs at Collector 1 and Chassis are measured again for all tests described in experiments 3.A.5.2 and 3.A.5.3 for comparison. The testing protocol is the same as the procedures mentioned in the 3.A.5.2. The recorded results all showed 0 V floating potentials, and no variations were detected as RF power and frequency varied.

The recorded SSFPs for experiments 3.A.5.1 and 3.A.5.2 are plotted with the power absorbed by the ETM P_{Fwd} in Fig. 13. At an absorbed power P_{Fwd} of 0.033 W (P_{out} of 0.105 W), the SSFP is -15.9 V at Collector 1, while the SSFP is -20.8 V at the Chassis. Both are much more negative than -13.5 V, the reference SSFP at both Collector 1 and Chassis solely due to the incoming electron beam. The more negative floating potentials at the electrodes are a solid indication of electron densification in the trapping region, as larger electrode-electron repulsive forces are needed to balance higher inter-electron repulsive forces generated in a densified electron cloud. Furthermore, the SSFP at the Chassis is more negative than the SSFP at Collector 1. This result further supports the conclusion that a more negative DC floating potential corresponds to a higher electron density: the U-shaped metal Chassis, sandwiched by two RF electrodes, has three sides immediately adjacent to the RF electron trapping region, while Collector 1 only covers the remaining side of the trap and is ≈ 3 millimeters further away from the trap. Thus, the Chassis, which is physically closer to the trapping region, has more area surrounding the electron trap than Collector 1.

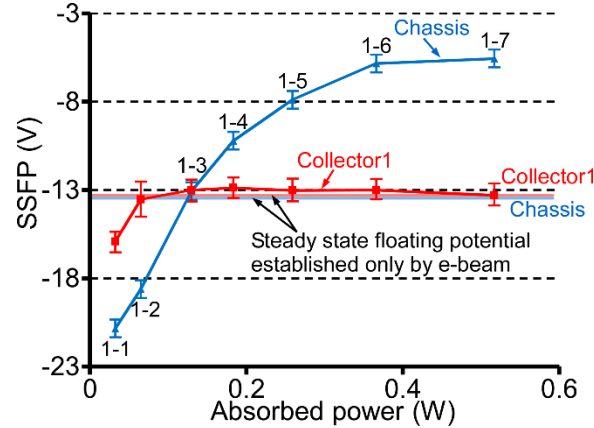


Fig. 13: The SSFPs measured across the capacitors in series with the Collector 1 and Chassis electrodes during RF electron trapping at different RF power levels with a fixed RF frequency of 143.6 MHz. The horizontal lines represent the SSFP established across the respective capacitors with only the injection of the 40 μ A electron beam.

As P_{Fwd} increases, the SSFPs at Collector 1 and Chassis also become more positive, indicating a loss in trap efficiency. With further increases, the SSFPs become more positive than the reference SSFP results with no RF power applied. This indicates a smaller electron density in the trapping region due to the applied RF. Both of these observations are expected from the analytical model: as the RF voltage $|V_{RF}|$ becomes higher than $|V_{RF_perfect}|$, the incoming electrons are accelerated excessively and leave the trap before the voltage reverses.

The results of experiment 3.A.5.3 indicate that the SSFP is around -7 V at Chassis and -13 V at Collector 1 at five testing points in the frequency range from 141 MHz to 152.5 MHz at a fixed output RF power P_{out} of 0.836 W (Fig. 14). (At 143.6 MHz, this is calculated as an absorbed power of 0.259 W). Since the SSFPs are linked to electron density in the trapping region, this indicates the trap electron density is similar over a range of f_{RF} at approximately the same power level.

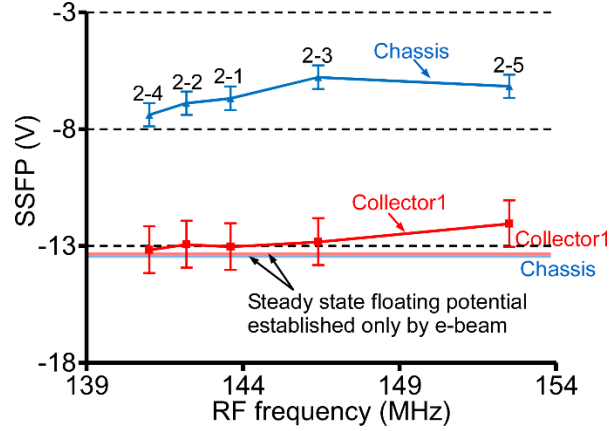


Fig. 14: The SSFPs across the capacitors associated with the Collector 1 and Chassis during RF trapping at different RF frequencies with a fixed output RF power of 0.836 W. The horizontal lines represent the SSFPs established across the respective capacitors with only the injection of electron beam.

3.A.6 – Ionization rate measurements

The ETM has successfully demonstrated the RF electron trapping concept to enable electrons to oscillate in longer trajectories, which results in much higher probability for the electron to collide with gas molecules at ultra-high vacuum levels. The next step is to demonstrate that the RF trapped and accelerated electrons have sufficient kinetic energy to ionize gas molecules. According to the kinetic theory of gases [Ser11], the estimated ion life time is approximately 2.5 μs for this specific 7 mm trap under the assumptions that all the ions are helium, and are drained out at root-mean-square speed of helium from the center of the trap to the electrodes at the edges of the trap. An experimental testing configuration (Fig. 15) has been developed to investigate the gas ionization of the ETM at the various RF signal levels which were identified previously to form the most effective RF electron traps.

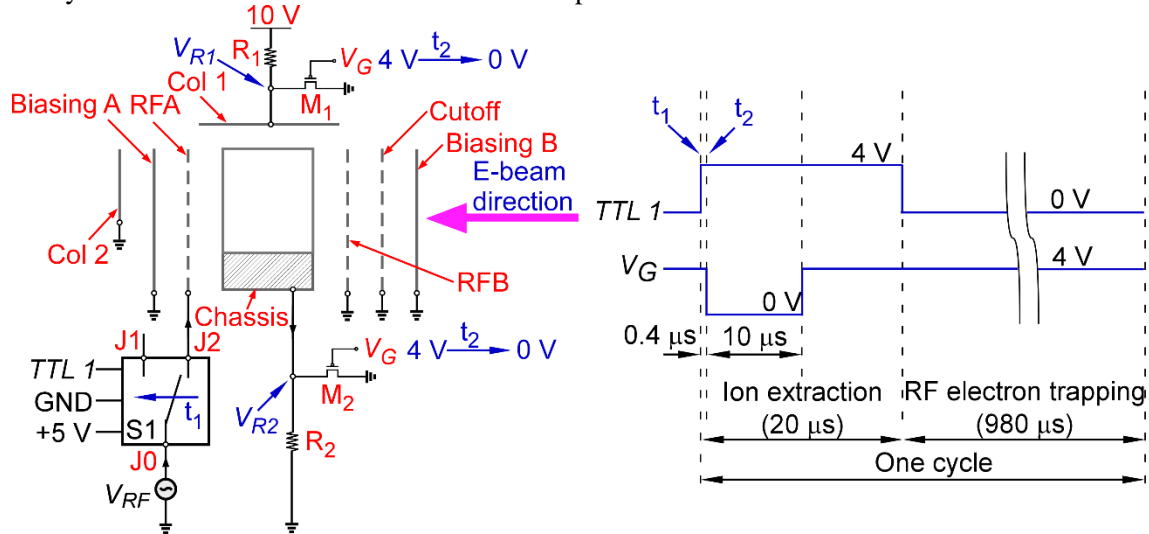


Fig. 15: (Left) The testing configuration to investigate the gas ionization of the ETM. R_1 is a 150 Ω high power resistor (Caddock Electronics MP915-150-1%, 15 W rated power), and R_2 is a standard 1 M Ω resistor. (Right) Timing diagram of the control voltages at TTL port of the high power RF switch (S1) and gates of two Power MOSFETs (M1 and M2) during one ion extraction and RF electron trapping cycle.

This testing configuration utilizes two operation states: an ion extraction state and an RF electron trapping state. A high power RF switch S1 (RF-LAMBDA RFSP2TRDC06G, DC-6 GHz, 5 W rated RF power, 70 ns switching speed, <0.5 dB insertion loss, >50 dB isolation) is located between the RF power source and the ETM. This element can switch the RF signal in and out of the ETM to transition between the two states. *Ion extraction state*: The RF signal is switched out of the ETM (S1 output port is switched

from J2 to J1) when *TTL 1* of S1 is changed from 0 V to 4 V at time t_1 . The gate voltage V_G of two Power MOSFETs M1 and M2 (VISHAY Si4124DY, $<0.001\ \Omega$ on-resistance, 40 V maximum drain-source voltage, >20 A continuous drain current) is triggered by *TTL 1* with a $0.4\ \mu\text{s}$ delay to change from 4 V to 0 V at time t_2 . This results in turning off both M1 and M2 transistors, and thus the voltage at Collector 1 V_{R1} is pulled up to 10 V to repel ions toward the Chassis, while the extracted ion current is passed through a $10\ \text{M}\Omega$ resistor R_2 . *RF electron trapping state*: After a $20\ \mu\text{s}$ ion extraction period, *TTL 1* of S1 is changed from 4 V back to 0 V (S1 output port is switched from J1 back to J2) to power the ETM with RF signal again, and M1 and M2 are turned on to force both Collector 1 and Chassis to ground potential at this time. This $980\ \mu\text{s}$ RF electron trapping period is sufficient to re-establish a stable RF electron trap for ionizing gas molecules according to the numerical modeling described in Task B of this report.

In this way, ions can be accelerated toward the Chassis by electrical potential less than $0.5\ \mu\text{s}$ after switching out the RF signal, and sensed without the interference of RF feedthrough current. The estimated ion extraction current is around $1\ \mu\text{A}$ under the assumptions that ion density is the same as the HPEM simulated electron density inside the trap, and all ions are extracted within a $20\ \text{ns}$ time frame. A $1\ \text{V}$ voltage V_{R2} across R_2 due to this ion current is expected to occur around $0.6\ \mu\text{s}$ after t_2 .

This approach and variations on it have been experimentally evaluated. In every variation, issues with voltage noise, charge injection from the switches, RF feedthrough, and/or timing constraints prevented any useful measurements of ionization. There are specific details of this scheme that may be causing this. First of all, any noise that is higher than the estimated ion current level can be a significant problem during ion current acquisition. Potential noise sources can come from the 5 V power supply and *TTL 1* of S1, for example. Another risk is that this scheme may not result in perfect grounding of Collector 1 and Chassis during the RF electron trapping state, as large RF feedthrough currents are capacitively coupled from RFA to other electrodes and the transistors M1 and M2 may not have very low impedance at these frequencies. Any RF voltage swing generated at the Chassis and Collector 1 may apply lateral Lorentz forces to the electrons and degrade the electron trap. Although the identified Power MOSFETs have small on-resistance ($<0.001\ \Omega$), their RF behavior has not been studied yet.

3.A.7 – Second generation device – Enhanced efficiency electron trapping module

This work concerns the design and fabrication of an enhanced-efficiency electron trapping module (E^3TM) that can fit into a $1.33''$ spherical vacuum chamber with only $16\ \text{cc}$ internal volume to demonstrate improved RF electron trapping. Other elements of this design are intended to allow demonstration of ionization and pumping of gases. The E^3TM consists of two titanium grid electrodes, and a tantalum sorption layer. The basic structure still follows the stacked and bolted architecture utilized in the ETM. However, there are several advantages incorporated in the design of the E^3TM compared to the ETM. First, customized titanium RF electrodes with a finer perforation pattern are designed to enable more uniform electric fields and a higher electron trapping efficiency, and to allow sputtering of fresh titanium which aids in gettering of reactive gases. A tantalum sorption layer is stacked into the E^3TM to enhance noble gas pumping via physical burial. Through some structural modifications, the effective pumping volume to device volume ratio is increased from 10.2% for the ETM to 51.7% for E^3TM while keeping the effective pumping volume the same. In addition, fewer metal electrodes are stacked into the E^3TM to reduce parasitics and simplify RF characterization. A smaller exposed area of isolating ceramic layers are used to minimize unwanted electron charge accumulation. Ultimately, the device electrical and mechanical connections are realized by directly building the E^3TM on top of a $1.33''$ ($3.38\ \text{cm}$) CF electrical feedthrough.

Structural design: The E^3TM is built and assembled on top of a 9-pin, subminiature-C $1.33''$ CF feedthrough as shown schematically in Fig. 16. The electrical connections and mechanical connections are realized by socket contact pins pushed on the feedthrough pins, so there is no need for additional mechanical support, and no need for vacuum-degrading soldering for electrical connections. The E^3TM along with the feedthrough is capable of “plugging” into the vacuum chamber, so no manipulation inside the chamber is needed. This enables a smaller vacuum chamber which minimizes outgassing from the internal surfaces of the chamber. All functional layers - two grid electrodes and the sorption layer - are in the same $15\ \text{mm}$

diameter circular shape to maximize the space utilization inside the vacuum chamber. The two grid electrodes are spaced 7 mm apart by three pillars placed at the periphery of the electrodes, rather than a U-shaped metal layer (Chassis) as used in the ETM. This results in better volume utilization in the E³TM. A spreading stand is added into the stack to fit the feedthrough pin arrangement on one side, while spreading the three pillars used to connect all layers together toward the edge of the circular layers. Furthermore, the electrical isolation is realized by putting small ceramic washers in between metal layers, instead of ceramic sheets as used in the ETM. This reduces the overall exposed ceramic surface in the vacuum chamber and should reduce charge accumulation while the electron beam is on. In addition, all non-essential metal layers in the ETM are removed to prevent parasitic inductances and capacitances in the E³TM.

Material selection and fabrication processes: The grid electrodes with a fine perforation pattern are fabricated from 100 μm thick titanium sheet with photochemical machining (PCM) - a commercially available batch compatible lithographic approach [ASM89]. This enables the sputtering of titanium during the ion sorption stage, which will chemically react with and remove reactive gases like oxygen and nitrogen [Sak94]. The potential candidates for a sorption layer should allow helium to be implanted deeply at low implantation energy, while also possessing a low diffusion coefficient to avoid the release of implanted helium back into the vacuum chamber. However, these two characteristics typically oppose each other. Tantalum is identified as a good sorption material candidate because it can realize a good balance between helium penetration depth and helium diffusibility [Zie03, Tro14, Sci83, Fla04]. The tantalum sorption layer is patterned with micro electrical discharge machining (μEDM) from a 200 μm thick, 15 mm diameter tantalum disk (Goodfellow, 012-928-68) [Mas90].

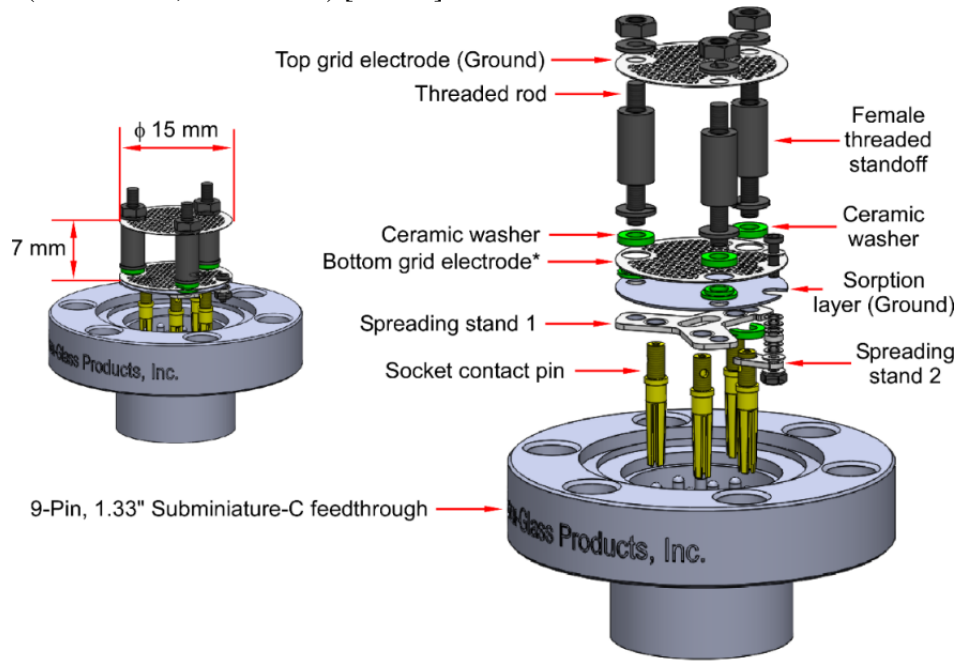


Fig. 16: The E³TM consists of two titanium grid electrodes and a tantalum sorption layer, and is built on top of a 9-pin, subminiature-C 1.33" CF feedthrough. *Indicates that the bottom grid electrode is the powered RF and pulsed DC electrode.

3.A.8 – Fabricated and assembled E³TM

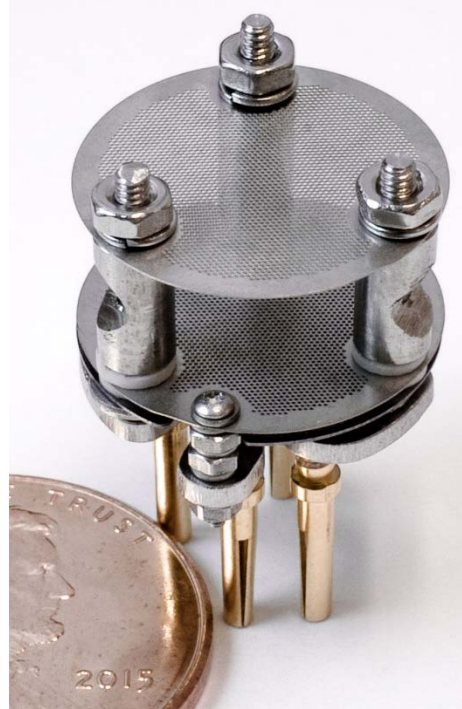


Fig. 17: Fabricated and assembled E³TM.

3.A.9 – Modification of vacuum testing setup

The overall internal volume of the vacuum setup identified previously is too large for pumping demonstration, because such a large surface area can result in a rapid increase in the vacuum level (to milliTorr level) due to extensive outgassing [Ota91]. However, several modifications can be made to append a small vacuum chamber to the larger chamber and still make full use of the already-built vacuum setup (Fig. 18).

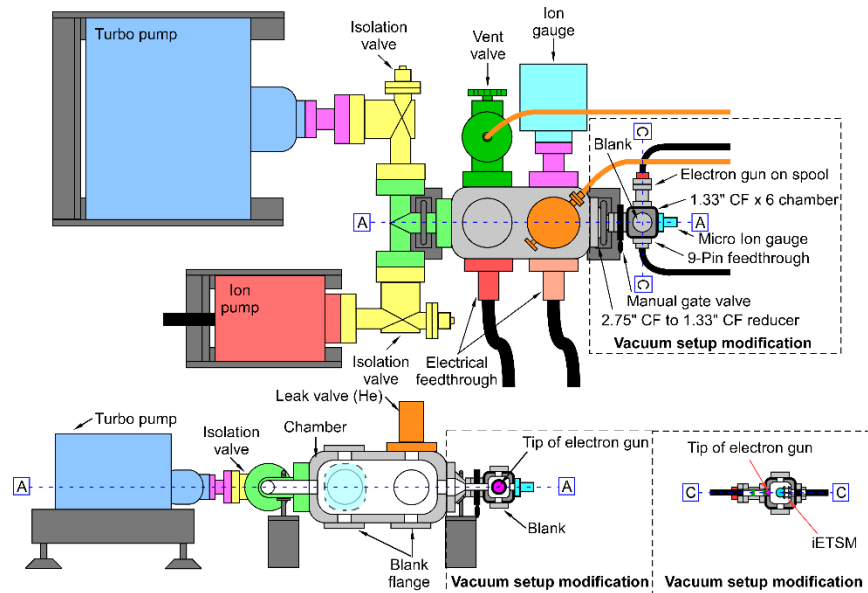


Fig. 18: The modified vacuum setup for E³TM is shown in the dashed box. Two cross sectional views (A-A, and C-C) are used to indicate relative position between different vacuum components.

Smaller vacuum chamber: By detaching the electron gun with 150 mm insertion length from the larger vacuum chamber, a 1.33" spherical cube chamber with only 16 cc internal volume (Kimball Physics, MCF133-SphCube-A6) can be attached to the larger chamber with a 2.75" CF to 1.33" CF reducer (Kimball Physics, MCF275-FlgAdptr-C1A1). The small vacuum chamber is manually isolated from the rest of the vacuum setup by a 1.33" CF gate valve (Ideal vacuum, 11120-0060). In this way, the commercial vacuum pumps can still be utilized to pump the smaller chamber to the pressure starting point for pumping demonstration testing. *Micro ion gauge:* A low power micro ion gauge with small dead volume (11 cc) (MKS/Granville Phillips, 355001-YF) is added to the small chamber to monitor pressure during pumping testing. *Customized electron gun:* A customized electron gun (Fig. 19) is designed by Kimball Physics to supply electrons for the E³TM. The insertion length of the new electron gun is reduced from 6" (15.24 cm) to 1.62" (4.12 cm), and is pre-assembled on a 1.4" (3.56 cm) long spool to enable a 0.22" (0.56 cm) insertion into the small chamber. Although another 16 cc of dead volume is added to the vacuum system with this approach, this does provide a robust and controllable electron source for the E³TM. *Electrical feedthrough:* A 9-pin, subminiature-C 1.33" CF feedthrough (Accuglass, 9C-133 100010) is used as the electrical feedthrough to provide mechanical support and electrical access for the E³TM. As a final note, all vacuum components, as well as the E³TM, are fully bakeable up to 250 °C, since an outgassing process may be needed before pumping testing to degas absorbed gas molecules from any surface inside the small chamber [Ich99].

The characterization of the E³TM is forthcoming but results have not been obtained in time for this report.

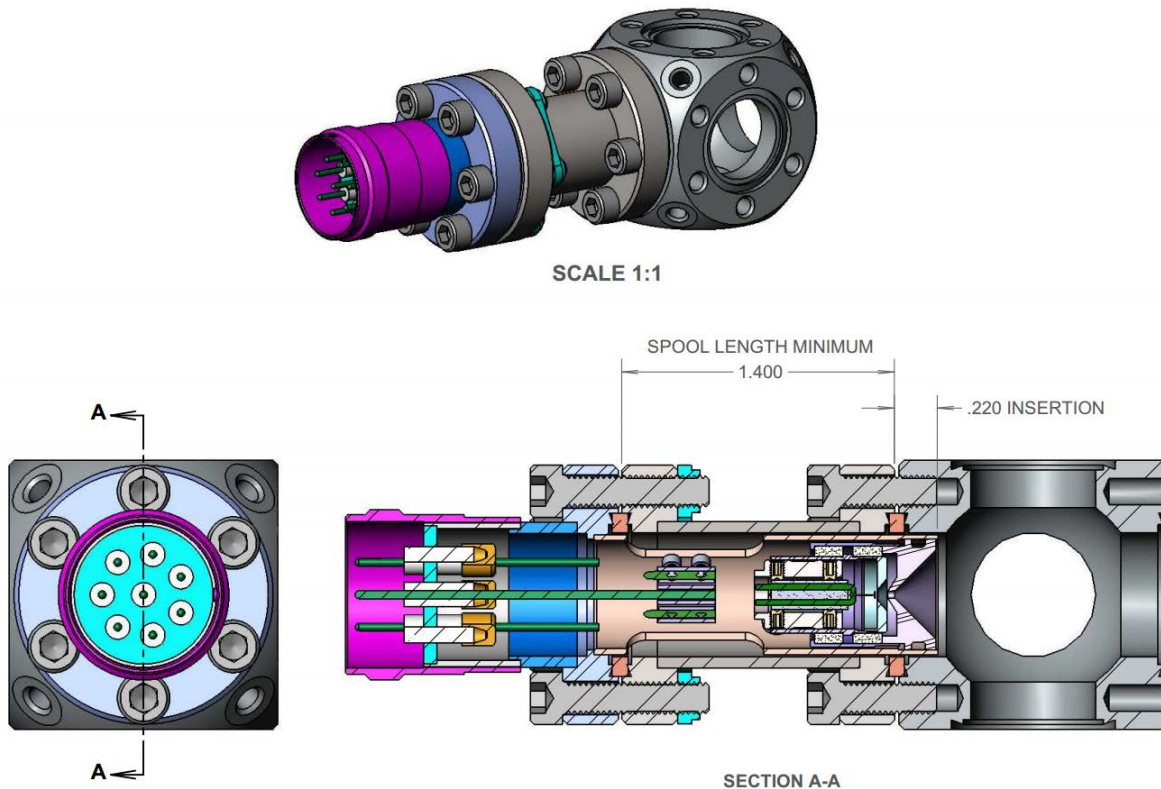


Fig. 19: Customized electron gun along with the 1.33" spherical cube vacuum chamber (drawing provided by Kimball Physics).

3.B Task B – Detailed numerical and parametric modeling

- Task B Objectives

- Establish appropriate algorithms and time/geometrical discretization in Hybrid Plasma Equipment Modeling code to deal with RF frequencies and miniaturized device volumes
- Produce numerical estimates of electron trapping and ionization rates for a nominal case
- Evaluate changes in electron trapping and ionization rates as parameters – such as frequency, voltage, pressure, beam current, beam energy – vary.
- Work toward applying lessons learned in the predictive design of second generation devices.

- Task B Accomplishments

3.B.1 – Model description

The Hybrid Plasma Equipment Model (HPEM) modeling framework was used to simulate the electron trapping in helium. The HPEM is a two-dimensional fluid-hybrid plasma simulation platform which has been previously described in detail in [Kus09]. The HPEM consists of separate modules, each of which addresses different physical phenomena and exchanges information between the modules in a hierarchical manner. The modules are executed sequentially on time scales short enough to resolve pulsed periods. A single execution cycle through all modules used in a simulation, with each module accepting data from the previous module and providing data for the next in a sequential manner, is called an iteration. The modules are cycled through until a convergence is reached or a specified number of iterations have occurred. In this study, the modules of HPEM utilized are the Fluid Kinetics-Poisson Module (FKPM), Electron Energy Transport Module (EETM) and Electron Monte Carlo Simulation (EMCS).

The densities of all charged and neutral species, and the electric potential are calculated in FKPM. For all species in the system (electrons, ions, and neutrals), continuity and momentum equations are integrated in time. The electric potential is obtained by solution of Poisson's equation using an incomplete LU BiConjugate Gradient sparse matrix solver. Charge densities on surfaces are computed as being due to the fluxes of electrons and ions from the bulk plasma and secondary electrons from other locations collected by those surfaces. A finite volume technique was used to discretize all spatial derivatives.

The Electron Monte Carlo Simulation (EMCS) within the EETM is used to derive electron energy distributions (EEDs) for both bulk electrons and for the transport of electrons from the beam source. The algorithms used in the EMCS are discussed in detail in [Kus09]. Briefly, electric fields from the FKPM are recorded as a function of position and phase during the RF cycle and cycle-averaged densities and source functions from the FKPM are then used to advance trajectories of electron pseudo-particles in the EMCS. Statistics are collected on the position and energy of electrons on each advance of their trajectories to produce EEDs, which are then combined with the electron densities from the FKPM to produce electron impact sources as a function of position. The electric field is updated when the FKPM and EETM are sequentially and iteratively called during execution of the model. The EMCS is also used to compute separate electron impact source functions resulting from the electron beam source. The secondary electrons are produced by fluxes of ions and excited states, which are obtained from the FKPM. The electrons that fall in energy below ≈ 4 eV are removed from the EMCS and are then treated in the bulk electron continuity equation.

The model developed in this study is computationally intensive. The model solves for plasma and neutral transport, temperatures and Poisson's equation using a combination of explicit, semi-implicit and implicit methods with time steps calculated based on instantaneous plasma properties or a fraction of the RF cycle. In order to benefit from multicore computer architectures, algorithms in the HPEM were parallelized using OpenMP directives. Since the HPEM consists of many different modules each having separate algorithms which are executed sequentially for relatively short times, it is difficult to amortize the computational overhead in launching parallel threads. For this particular implementation of the HPEM, the overall speedup gained with respect to serial execution is shown in Fig. 20, and is 2.6 on 12 cores using the Intel Fortran Compiler and 2.8 GHz Intel Xeon processors.

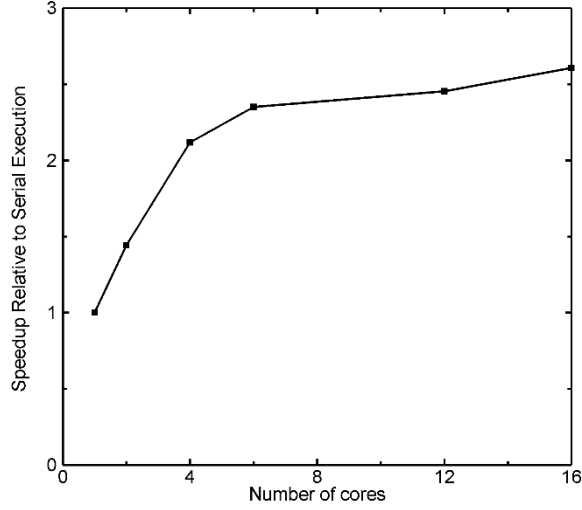


Fig. 20: Speedup in HPEM code solutions via multi-core processing.

In figure 21 a schematic of the geometry used in modeling of the electron trap is shown. Two gridded electrodes are separated by ceramic/grounded metal/ceramic spacers making the walls of the electron trap with dimensions of 0.7 cm tall x 1 cm wide. The ceramic spacer has a thickness of 1 mm and 6.8 relative permittivity. The top electrode is RF powered, while the bottom one is grounded. The grid consists of rectangular blocks with dimensions of 0.5 mm tall x 1 mm wide, which are separated by 1.75 mm voids. The electrons are injected into the intra-grid (trapping) region from an electron beam source (0.8 cm wide) located at the bottom of the domain, 1 cm below the grounded electrode. The computational domain, 3.4 cm tall x 1.8 cm wide, is discretized in a Cartesian coordinate system on a grid of 140 by 75 cells and assumes symmetry about the central y-axis.

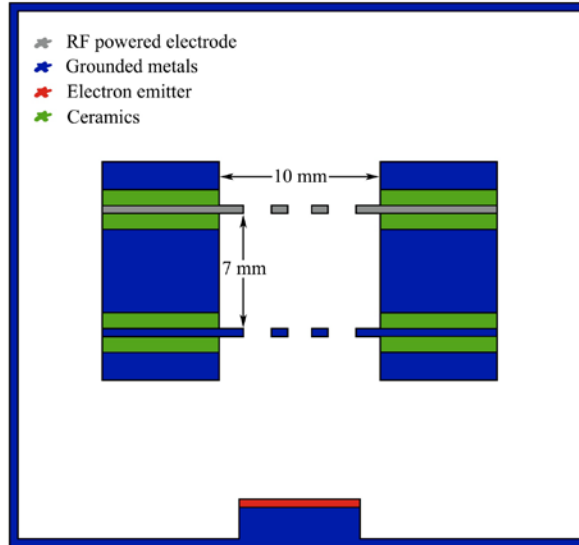


Fig. 21: Schematic of the electron trap geometry used in the HPEM model.

The first-principles model described in 3.A.1 analyzes a simplified and idealized case. Despite many assumptions, the model can provide insight into the efficiency of the trap. Based on this analysis and power budget for the experimental device, a parameter range is established in which electron trapping should be established with an RF modulated electric field. This parameter range is investigated with the HPEM model. In the nominal case, the computational domain is filled with 80 nTorr helium at room temperature.

The top electrode is powered by 150 V RF potential oscillating at 150 MHz RF frequency. The electron beam provides a uniform electron flux of 40 μA per 0.8 cm with 15 eV initial electron temperature.

3.B.2 – Results

In figure 22 the cycle averaged electron and helium ion densities are shown for the nominal case. Both densities are concentrated in the intra-grid region (trapping region or trap). Electrons injected from the electron beam, having initial 15 eV energy, travel to the grounded electrode and depending on the current phase of RF will be rejected or trapped. Trapped electrons oscillate in the trap before hitting and ionizing helium molecules or hitting the walls and disappearing. Based on simple analysis, electron excursion time (the number of cycles an electron will survive before hitting the wall or going out of trap) depends on the electron energy at the grounded electrode and the phase of RF at that instance. The longer the excursion time, the higher probability of collision with a helium molecule. In order for the collision to be an ionization event, the electron energy at collision should be at least as high as the ionization threshold in helium, which is 24.58 eV. Electron density is built on a cycle to cycle basis and reaches periodic steady state within tens of cycles. Steady state peak electron density is 3 orders of magnitude higher than the initial electron density.

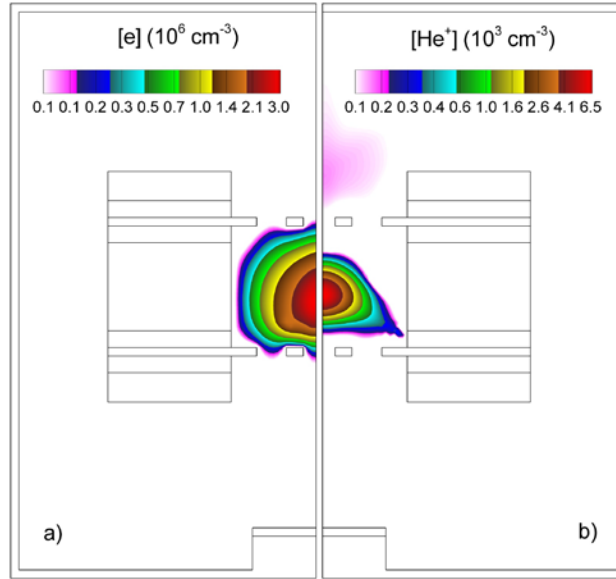


Fig. 22: Plasma properties for the nominal case conditions (He, 80 nTorr, 150 MHz, 150 V, 15 eV, 40 μA). (a) Electron density and (b) He+ density.

Electron impact ionization sources due to the bulk S_{bulk} and electron beam S_{ebeam} are shown in figure 23. The profile of S_{bulk} mirrors the profile of electron density and peaks at $6.1 \times 10^6 \text{ cm}^{-3} \text{ s}^{-1}$. The trajectories of electrons from the electron beam are vertical, perpendicular to the surface of the electron beam source. As a result, S_{ebeam} shows mostly vertical traces with horizontal scattering in the region above the powered electrode. S_{ebeam} peaks in the trap with a value of $89.5 \times 10^6 \text{ cm}^{-3} \text{ s}^{-1}$. The synergistic effect of the electron beam source and the RF modulated field results in the efficient trapping of electrons in the intra-grid region.

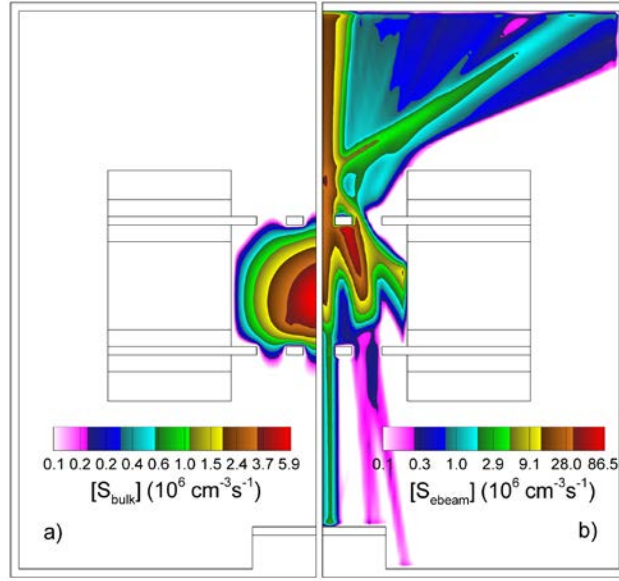


Fig. 23: Plasma properties for the nominal case conditions (He, 80 nTorr, 150 MHz, 150 V, 15 eV, 40 μA). Electron impact ionization source by (a) bulk and (b) electron beam electrons.

In figure 24, the base pressure is varied to 40 nTorr and 120 nTorr. We show the results of electron density and S_{bulk} on the centerline ($x = 0 \text{ cm}$). The electron density is not sensitive to pressure changes, while S_{bulk} scales linearly with pressure.

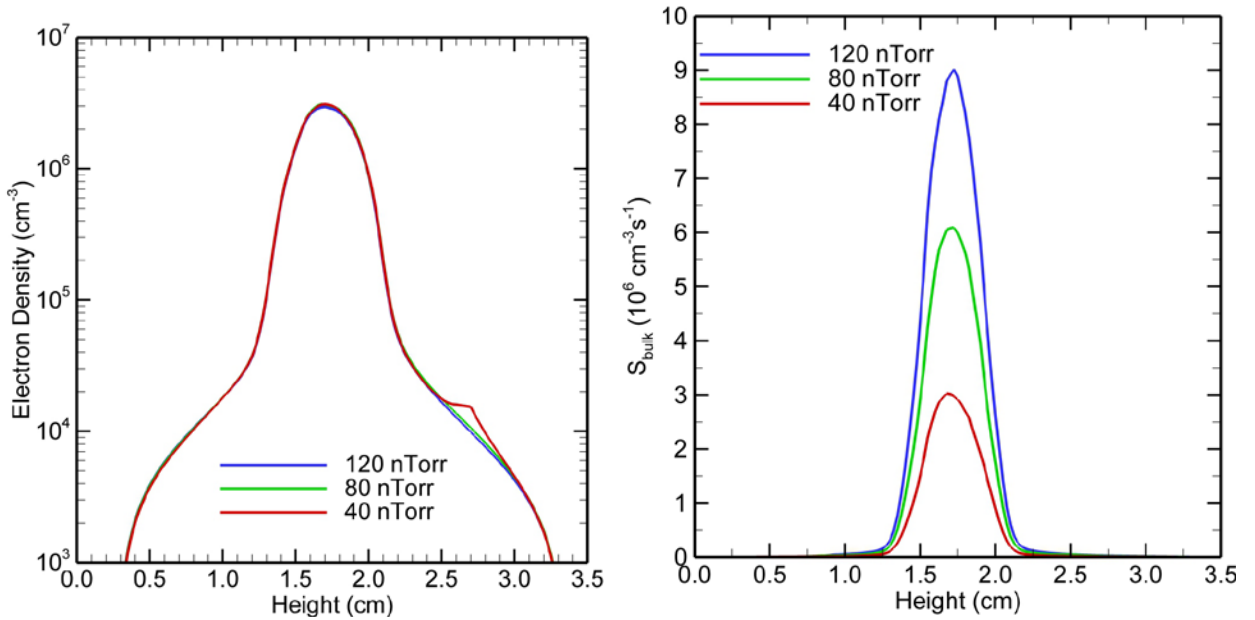


Fig. 24: Electron trapping for gas pressures of 40, 80, and 120 nTorr (He, 150 MHz, 150 V, 15 eV, 40 μA). (left) Electron densities and (right) electron impact ionization sources by bulk electrons along the vertical midline of the trap ($x = 0 \text{ cm}$ in the modeled domain).

The initial energy of electrons injected from the electron beam source is varied between 5, 15, 30 and 60 eV in figure 25. With increasing electron energy, the ionization sources S_{ebeam} are distributed fairly uniformly over the entire region in front of the electron beam source. In the case of low initial electron

energies up to 15 eV, the electrons are not energetic enough to overcome the ionization threshold in the area between the electron beam source and grounded electrode, as well as in the lower half of the electron trap. For increased initial energies from 30 eV and higher, the energy is sufficient to produce an ionization event in the regions directly in front of the beam source. However, the ionization event density is still larger within the trap for these energies.

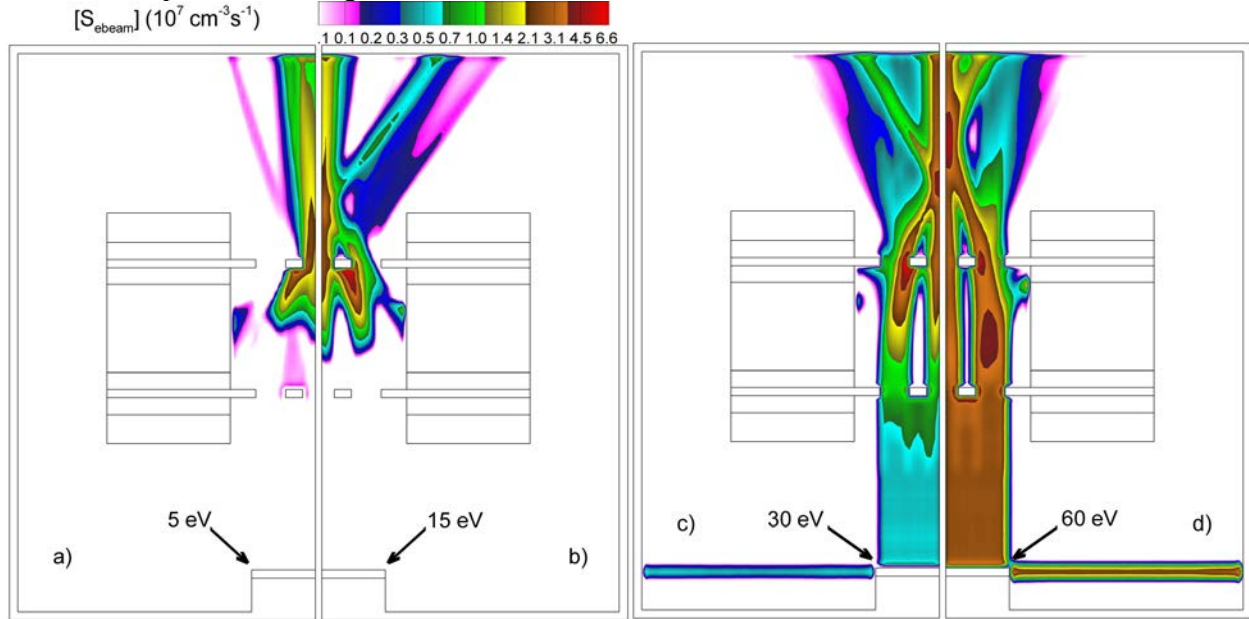


Fig. 25: Electron impact ionization sources by beam electrons for the initial beam energies of (a) 5 eV, (b) 15 eV, (c) 30 eV, and (d) 60 eV (He, 80 nTorr, 150 MHz, 150 V, 40 μ A).

The trapped electron density is highly sensitive to the electron beam current. Figure 26 shows the electron density on the centerline ($x = 0$ cm) for various currents of 20–2000 μ A and peak electron density as a function of the current. Peak electron density varies with electron beam current fairly linearly over this range of current.

Figure 27 shows the peak electron density in the trap as a function of RF voltage for the fixed frequency of 150 MHz. The peak electron density has the highest values for the voltages between 100 and 200 V. It is remarkable that the electron density in the case of 1000 V is 6 times lower than for the values at 200 V. The figure should be viewed in conjunction with figure 28, where the peak electron densities in the trap for various fixed frequencies as a function of k_f are shown (the voltages vary as in the x-axis of figure 27). In the case of 150 MHz, the peak value is reported for k_f values from 1 to 1.6 (which corresponds to the voltages of 100 to 200 V), which is in good agreement with the predictions of the analysis presented in 3.A.1. These trends are in a good agreement with experimental observations. For the other values of the frequencies, the trends do not fully obey the predictions from the first-principles analysis. The peaks are mostly occurring when voltages are between 100 to 250 V, while corresponding k_f values are scattered between 0.3 and 1.7. The disagreement between the simplified analysis and the simulation results in figure 28 is likely due to a number of effects not captured in the simplified analysis: electric field non-uniformity, repulsion from charged surfaces, electrons generated via ionization events, etc.

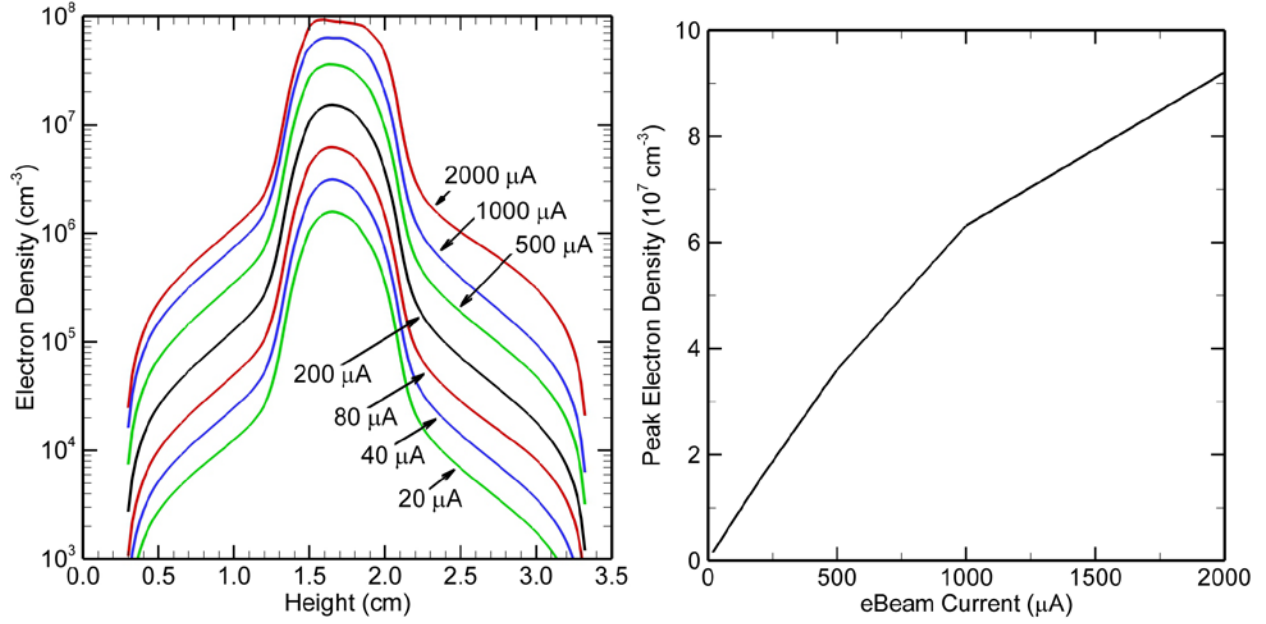


Fig. 26: (left) Electron densities as a function of height on $x = 0$ cm for different electron beam currents. (right) Peak electron density as a function of electron beam current (He, 80 nTorr, 150 MHz, 150 V).

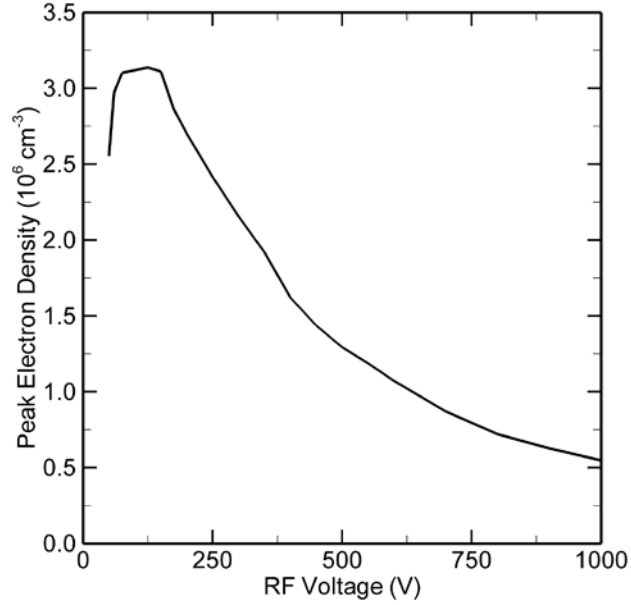


Fig. 27: Peak electron density as a function of applied RF voltage (He, 80 nTorr, 150 MHz, 15 eV, 40 μA).

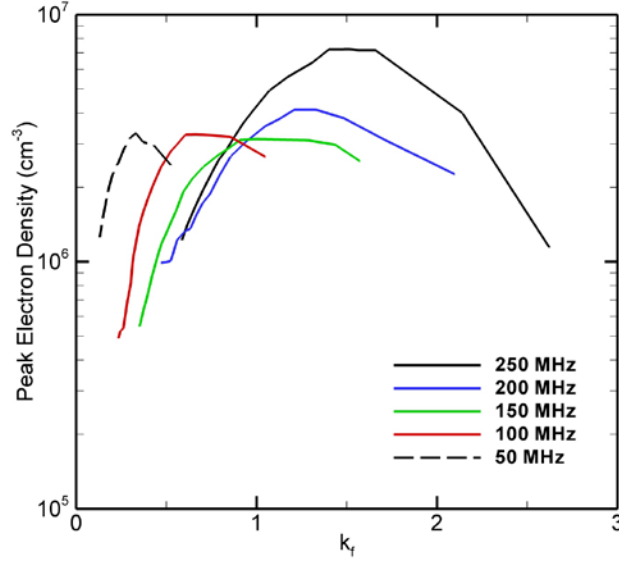


Fig. 28: Peak electron density as a function of k_r for RF frequencies of 50, 100, 150, 200, and 250 MHz (He, 80 nTorr, 15 eV, 40 μ A).

4.0 Conclusions

There are several conclusions that can be drawn from the efforts described. First, the device structure is effective in trapping electrons at nanotorr pressure levels using only RF. The DC floating potential measurement scheme, which correlates the SSFPs established across DC blocking capacitors with electron density in trapping region, was developed to investigate RF electron trapping in the ETM. At an absorbed RF power P_{Fwd} of 0.033 W at RF frequency f_{RF} of 143.6 MHz, the measured SSFP at Chassis and Collector 1 were more negative than reference SSFP with RF power off and only due to the injection of electron beam. This demonstrated that the electron density over the trapping region was increased by this applied RF signal, and proved the RF electron trapping concept. Further, as P_{Fwd} rose above 0.259 W (143.6 MHz), which is a power level that would result in a RF voltage $|V_{RF}|$ too high to effectively trap electrons according to the analytical model, the SSFPs at Chassis and Collector 1 became more positive than reference SSFP results. This indicated a lower electron density with the presence of RF signal at that power level, and demonstrated that effective RF electron trapping can only happen over a certain RF power range at a specific RF frequency. Finally, the SSFPs at Chassis and Collector 1 remained stable over a range of f_{RF} at a fixed output RF power P_{out} of 0.836 W. This matched the Hybrid Plasma Equipment Model (HPEM) results that showed the same electron densification could occur over a range of f_{RF} .

While ionization measurement from the ETM has been constrained by noise and electrical parasitics, the HPEM modeling does indicate that sufficient ionization can occur in this type of device. The second generation device, an enhanced-efficiency electron trapping module (E³TM), has been designed and assembled. The improvements designed into this device, as well as the modified test chamber, are anticipated to allow the demonstration of efficient RF electron trapping, sorption, and pressure modulation in the coming few months.

5.0 Discussion and future potential

This work was the first to investigate RF electron trapping between planar electrodes as part of a magnet-less ion pumping concept. The experimental work and numerical modeling done on proof-of-concept devices illustrate with certainty that electrons can be trapped with this approach. It is also clear that this approach has advantages over other magnet-less electron-ionization approaches. First, the trap can densify electrons by at least three orders of magnitude; this can enable reduced electron current from field

emitters or other electron sources, which will lower tip heating, outgassing, and electron source degradation compared to approaches that do not trap electrons. Second, this trap has been shown through modeling to utilize a large portion of the intra-grid volume for trapping and ionization; other trapping approaches may utilize only specific trajectories within the trapping space and thus be less volume efficient than this approach. Finally, this trap has also been shown through modeling to be fairly insensitive to incoming electron energy; other trapping approaches that rely on establishing orbits may be very sensitive to this parameter. The work described in this report has also shown that a major risk with this approach – power draw during RF trapping – can be mitigated by taking advantage of serial resonances within the device. Results from the first generation device described here indicate that further attention to RF design and minimization of parasitic resistances may allow continuous RF duty at ~10 mW of power in a device of this size.

This work has established the suitability of the RF electron trapping approach, and the promise of a miniaturized, magnet-less ion pump. Results from the second generation device (E³TM) are forthcoming. The approach itself has many built-in features that should improve pumping: the ability to handle gases besides helium via sputtering of the titanium electrodes, a triode configuration that should protect delicate pump components like field emitter tips, and an integrated low dead-volume ion pressure gauge that can enable servo-controlled pressure modulation. Work beyond the first pumping demonstrations will yet be required: integration of a robust electron source, implementation of board-or-chip-level power and control electronics, and demonstration of full compatibility with atomic microsystems. Further miniaturization of this pump may be possible, especially by implementing microfabrication processes. However, new methods may be required to accommodate the parasitic capacitances that may become more dominant as electrode gaps are reduced.

Acknowledgments

This material is based on research sponsored by the Air Force Research Laboratory under agreement number FA9453-14-1-0347. The investigators thank Dr. Robert Lutwak of DARPA MTO for his support. The U.S. Government is authorized to reproduce and distribute reprints for Governmental purposes notwithstanding any copyright notation thereon.

List of Patents

None

List of Publications

None (two manuscripts in preparation)

List of Public Presentations (including DoD or DARPA presentations)

“RF-Trapped Chip-Scale Helium Ion Pump”, DARPA’s microPNT PI Review, San Antonio, TX, November 2014

“RF-Trapped Chip-Scale Helium Ion Pump”, DARPA’s microPNT PI Review, Pittsburgh, PA, April 2015

“RF-Trapped Chip-Scale Helium Ion Pump”, DARPA’s microPNT PI Review, San Diego, CA, October 2015

“Miniaturized Magnet-Free Ion Pumps for Ultra High Vacuum”, DARPA’s ACES Proposers Day, Arlington, VA, February 2016

List of Poster Presentations (including DoD or DARPA presentations)

“RF-Trapped Chip-Scale Helium Ion Pump”, DARPA’s microPNT PI Review, San Antonio, TX, November 2014

“RF-Trapped Chip-Scale Helium Ion Pump”, DARPA’s microPNT PI Review, Pittsburgh, PA, April 2015

“RF-Trapped Chip-Scale Helium Ion Pump”, DARPA’s microPNT PI Review, San Diego, CA, October 2015

References

- [An13] S. An, N. K. Gupta, and Y. B. Gianchandani, "A Si-micromachined 162-stage two-part Knudsen pump for on-chip vacuum," *Journal of Microelectromechanical Systems*, vol. 23, pp. 406-416, 2014.
- [ASM89] ASM International, ASM Handbook, Materials Park, OH, 1989, vol. 16.
- [Aud87] M. Audi, and M. de Simon, "Ion pumps," *Vacuum*, vol 37, pp. 629-636, 1987.
- [Bor02] C. Borde, "Atomic Clocks and Inertial Sensors," *Metrologia*, vol. 39, pp. 435-463, 2002.
- [Fla04] J. L. Flament, F. Zielinski, S. Saudé, and R. I. Grynszpan, "Helium diffusion in metals investigated by nuclear reaction analysis," *Nuclear Instruments and Methods in Physics Research Section B: Beam Interactions with Materials and Atoms*, vol. 216, pp.161-166, 2004.
- [Gom94] R. Gomer, "Field emission, field ionization, and field desorption," *Surface Science*, vol. 299/300, pp. 129-52, 1994.
- [Gor80] A. van Gorkum, and E. Kornelsen, "The entrance probability and range of Helium in W (100) for energies 8 eV to 5000 eV as measured by thermal desorption spectrometry," *Radiation Effects*, vol. 52, pp. 25-33, 1980.
- [Gre13] S. R. Green, R. Malhotra, and Y. B. Gianchandani, "Sub-Torr Chip-Scale Sputter-Ion Pump Based on a Penning Cell Array Architecture," *Journal of Microelectromechanical Systems*, vol. 22, pp. 309-17, 2013.
- [Ich99] S. Ichimura, K. Kokubun, M. Hirata, S. Tsukahara, K. Saito, and Y. Ikeda, "Measurement of outgassing characteristics from a vacuum chamber fabricated for pressure calibration in UHV/XHV region," *Vacuum*, vol. 53, pp.291-294, 1999.
- [Kit11] J. Kitching, S. Knappe, and E. Donley, "Atomic Sensors – A Review," *IEEE Sensors Journal*, vol. 11, pp. 1749-1757, 2011.
- [Kus09] M. J. Kushner. Hybrid modelling of low temperature plasmas for fundamental investigations and equipment design. *J. Phys. D*, **42**(19):194013, 2009.
- [Lie94] M. Lieberman, and A. Lichtenberg, *Principles of Plasma Discharges and Materials Processing*, John Wiley & Sons, New York, NY; 1994.
- [Lie04] L. A. Liew, S. Knappe, J. Moreland, H. Robinson, L. Hollberg, and J. Kitching, "Micro-fabricated alkali atom vapor cells," *Applied Physics Letters*, vol 84, pp. 2694-2696, 2004.
- [Lut04] R. Lutwak, J. Deng, W. Riley, M. Varghese, J. Leblanc, G. Teplot, M. Mescher, D. Serkland, K. Geib, and G. Peake, "The chip-scale atomic clock – Low-power physics package," *36th Annual Precise Time and Time Interval (PTTI) Meeting*, pp. 339-354, 2004.
- [Mas90] T. Masaki, K. Kawata, and T. Masuzawa, "Micro electro-discharge machining and its applications," *Proc. IEEE Micro Electro Mechanical Systems: An Investigation of Micro Structures, Sensors, Actuators, Machines and Robots*, Napa Valley, CA, Feb. 1990, pp. 21-26.

- [Ota91] N. Ota, F. Watanabe, K. Kanazawa, T. Momose, and H. Ishimaru, "Outgassing-rate-measurement apparatus for small parts in ultrahigh vacuum," *Journal of Vacuum Science & Technology A*, vol. 9, pp.2771-2775, 1991.
- [Pan90] C. Pan, and H. Kelly, "Calculation of the electron-impact-ionization cross section of Helium including electron correlations," *Physical Review A*, vol. 41, pp. 3624-3634, 1990.
- [Qia09] C. Qian, and W. W. Brey, "Impedance matching with an adjustable segmented transmission line," *Journal of Magnetic Resonance*, vol. 199, pp. 104-110, 2009.
- [Ros62] D. Rosenberg, and G. Wehner, "Sputtering Yields for Low Energy He⁺, Kr⁺ and Xe⁺ Ion Bombardment," *Journal of Applied Physics*, vol. 33, pp. 1842-1845, 1962.
- [Sak94] G. L. Saksaganskii, *Getter and Getter-Ion Vacuum Pumps*, Harwood Academic, 1994.
- [Sci83] V. Sciani, and P. Jung, "Diffusion of helium in fcc metals," *Radiation Effects*, vol. 78, pp.87-99, 1983.
- [Ser11] R. A. Serway, and C. Vuille, *College physics*, Brooks/Cole, Boston, MA; 2011.
- [Sug98] M. Sugawara, *Plasma Etching: Fundamentals and Applications*, Oxford University Press Inc., New York, NY; 1998.
- [Tee05] T. Teepe, A. van Veen, H. van't Spijker, S. Steenbrink, A. van Zuuk, C. Heerkens, M. Wieland, N. van Druten, and P. Kruit, "Fabrication and characterization of p-type silicon field-emitter arrays for lithography," *Journal of Vacuum Science and Technology. B*, vol. 23pp. 359-369, 2005.
- [Tro14] P. Trocellier, S. Agarwal, and S. Miro, "A review on helium mobility in inorganic materials," *Journal of Nuclear Materials*, vol. 445, pp. 128-142, 2014.
- [Vel10] L. Velasquez-Garcia, B. Gassend, and A. I. Akinwande, "CNT-based MEMS ionizers for portable mass spectrometry applications," *Journal of Microelectromechanical Systems*, vol. 19, pp. 484- 493, 2010.
- [Wel01] K. M. Welch, *Capture Pumping Technology*, 2nd ed., Elsevier, 2001.
- [Win74] H.F. Winters, and P. Sigmund, "Sputtering of chemisorbed gas (nitrogen on tungsten) by low-energy ions," *J. Applied Physics*, vol. 45, pp.4760-4766, 1974.
- [Wri07] S. A. Wright, and Y. B. Gianchandani, "Controlling pressure in microsystem packages by on-chip microdischarges between thin-film titanium electrodes," *Journal of Vacuum Science and Technology. B*, vol. 25, pp. 1711-1720, 2007.
- [Zie03] F. Zielinski, J. M. Costantini, J. Haussy, and F. Durbin, "Helium depth profiling in tantalum after ion implantation and high-temperature annealing," *Journal of Nuclear Materials*, vol. 312, pp: 141-145, 2003.
- [Zoo92] J. Zook, D. Burns, H. Guckel, J. Sniegowski, R. Engelstad, and Z. Feng, "Characteristics of polysilicon resonant microbeams," *Sensors and Actuators A*, vol. 35, pp. 51-59, 1992.

DISTRIBUTION LIST

DTIC/OCF	
8725 John J. Kingman Rd, Suite 0944	
Ft Belvoir, VA 22060-6218	1 cy
AFRL/RVIL	
Kirtland AFB, NM 87117-5776	2 cys
Official Record Copy	
AFRL/RVBYE/Dr. Spencer E. Olson	1 cy